Title

Microtubule Nucleating complexes: A structural view

Author

Choy, Rebeca Maria

Publication Date

2013

Microtubule Nucleating Complexes: A structural view

by

Rebeca M. Choy

DISSERTATION

Submitted in partial satisfaction of the requirements for the degree of

DOCTOR OF PHILOSOPHY

in

Biophysics

in the

GRADUATE DIVISION

of the

UNIVERSITY OF CALIFORNIA, SAN FRANCISCO

[redacted]

Acknowledgements

Graduate school has been a great learning experience for me. During my tenure, I have met people that are not only excellent scientists, but they are also renaissance people. Their company has been very nourishing in every aspect of my life; I believe my life is more interesting thanks to them.

I would like to thank my advisor David Agard for all his sagely advice, patience and the environment he maintains in his laboratory. All of the students are very happy and eager to work. There is a sense of camaraderie and support among students, that extends to the postdocs, staff and Dave himself. David always advice me in all areas; forming hypotheses, experimental design, data collection and analysis.

I would like to thank my thesis committee: Yifan Cheng and Matthew Jacobson. Not only I have received advice related to my project, but in my professional life as well. They were always extremely approachable by fostering an peer-to-peer relationship.

When I started graduate school, I was not thinking on doing experimental biology; I have to thank Julie Ransom for encouraging to “experiment”. I feel a richer person thanks to that. Rebecca Brown has been a great replacement for Julie. Rebecca is a great source of help and advice.

Learning how to do experimental science would have been more of a headache if I wasn’t surrounded by excellent lab mates. Justin Kollman was the first person to taught me how to use a pipette and with whom I made my first protein prep and took a look at it on the EM. Michelle Moritz, taught me how patience and careful planning and can lead to great experiments. She is one of the best experimentalists I've met. Michelle also was extremely receptive of any question I had and was always eager to discuss any matter with me. I owe a lot to Sam Li. Sam taught me a lot about EM and helped me at every step of my cryo studies. He's one of the most knowledgeable scientists, in both biology and EM, I've met and he's also one of my best friends.

I also want to thank our long-term collaborators Trisha Davies and Eric Muller, which without I wouldn't have such a great experience at the beginning of my graduate career.

Shawn Zheng has been key for me to learn how to set up the EM for automated acquisitions. He's also was a great collaborator during the acquisition scheme work was set in place and he made it happen.

Sabine Petry is another great scientist that I had the pleasure to work with. We had a great collaboration and I learned a lot from her. Another collaborator that has swept me off my feet is Yi Shi. He's been a great collaborator and always full of ideas.

Mariano Tabios and Joyce Ramponi keep the lab in such a great shape. I think great science is fostered in the lab and they make it happen. Not only I appreciate the work they do, but they are also very good friends. My free time cannot be better spent.

Michael Braunfeld and Agustin Avila-Sakar helped me a lot in the EM. They always met my needs with great attitude and were always so didactic.

My current and former labmates, whom I have become friends with: Klim, Daniel, Laura, Liz, Elaine, Bosco, Ulrike, Kristin and JK. These kids made and make the lab and life very interesting. I hope we will still be in touch even though we're and will be far away!

My classmates who have turned into my best friends: Sai, Sheel and Jeremy. Thanks for all the fun times and support.

I would also want to thank my parents, Ana and Jose. Looking back at my earlier years, I can not thank my lucky stars that I was born in such a supportive and fair family.

Last, but not least, I would like to thank Steve. Without his blind support, I wouldn't be in graduate school. I'm lucky to have found a partner that helps me grow as a person, is always so much fun and it has a great social conscience. Thanks to him I'm a better person.

Microtubule nucleating complexes*: A structural view*

by

Rebeca M. Choy

Abstract

Microtubule Organizing Centers (MTOCs) organize the spatial and temporal patterns of microtubules by controlling their nucleation.

Microtubule nucleation is mediated by γ-Tubulin. From yeast to humans, γ-Tubulin is found in a ~300kDa protein complex called γ-Tubulin Small Complex or γTuSC. γTuSC assembles into a ~2.2MDa complex called γ-Tubulin Ring Complex (γTuRC) that nucleates Microtubules by providing a template from which protofilaments can nucleate.

The structure of the *S. cereviseae* γTuRC has been determined at a subnanometer resolution, indicating the organization of the γTuSC within the ring. While the overall structure of the γTuRC is conserved, in higher-eukaryotes γTuRC contains 5 more proteins (GCPs) than its yeast counterpart. Studies at the cell level indicate that these proteins are used as localization markers for γTuRCs within the cell. Structural work in one of the human non-γTuSC proteins has revealed a striking similarity to the yeast proteins indicating that the GCPs localize within the ring. Despite this indications, the organization of the GCPs within these complexes remains unclear.

The following manuscript details the work done in understanding the organization of the proteins that make up the *S. cereviseae* γTuSC and the first Cryo-Electron Microscopy structure of the *D. melanogaster* γTuRC.

The *S. cereviseae* work describes the orientation of the proteins within the complex which helped in understanding the sequence to structure role.

The structural work of the *D. melanogaster* γTuRC strengthens the theory of the localization of the extra GCPs and an initial indication of the stoichiometry of these components.

As part of the structural work on γTuRC, an acquisition paradigm was designed to speed up cryo-EM tomography data collection as well as significantly improving the data quality and resolution.

Table of Contents

List of Tables

Chapter I: ***An introduction to Microtubule Organizing Centers, Microtubules and Microtubule Nucleating Complexes***

Chapter III: ***Structure of the γ-Tubulin Ring Complex in D. melanogaster***

List of Figures

Chapter I: ***An introduction to Microtubule Organizing Centers, Microtubules and Microtubule Nucleating Complexes***

Chapter II: ***Localization and orientation of the γ-Tubulin Small Complex components using protein tags as labels for single particle EM***

Chapter III: ***Structure of the γ-Tubulin Ring Complex in D. melanogaster***

Chapter IV: ***Automated Data Collection for Single-Particle Electron Microscopy Tomography with Dose Fractionation***

Chapter I:

An introduction to Microtubule Organizing Centers, Microtubules and Microtubule Nucleating Complexes

On Microtubule Organizing Centers

Microtubule organizing centers (MTOCs) are organelles in the cell that provide a scaffold for cell structure. MTOCs organize the eukaryotic flagella and cilia, the interphase microtubule (MT) cytoskeleton and, they accurately segregate chromosomes during cell division. All of this is accomplished by anchoring, organizing and controlling nucleation of MTs.

Across eukaryotes, MTOCs have different morphologies, yet their function remains the same. This manuscript will be focused on metazoan and fungi MTOCs, more specifically *D. melanogaster and S. cerevisiae.*

In metazoans, the MTOC is called Centrosome and it has an arrangement as seen in Figure 1A. In a very condensed manner, the Centrosome organization can be described as follows. At the center of the Centrosome are the centrioles. Centrioles are responsible to recruit pericentral material (PCM), establish polarity during cell division, and normal mitosis progression (Nigg and Stearns 2011, Bornens 2012, Mahen and Venkitaraman 2012). Centrioles also become flagella and cilia in a tissue dependent manner (Ishikawa and Marshall 2011). Surrounding the centrioles is the PCM. The PCM is thought to have a structure composed of concentric layers of different proteins with distinct functions during the cell cycle (Bornens 2002, Mennella, Keszthelyi et al. 2012).

Figure 1: Metazoan and Fungi MTOCs. (A) Centrosome showing a simplified view of its parts. Figure adapted from Molecular Biology of the Cell, 4th Edition. (B) Spindle Pole Body showing a simplified view of its parts. Figure adapted from **(Jaspersen and Winey 2004)**

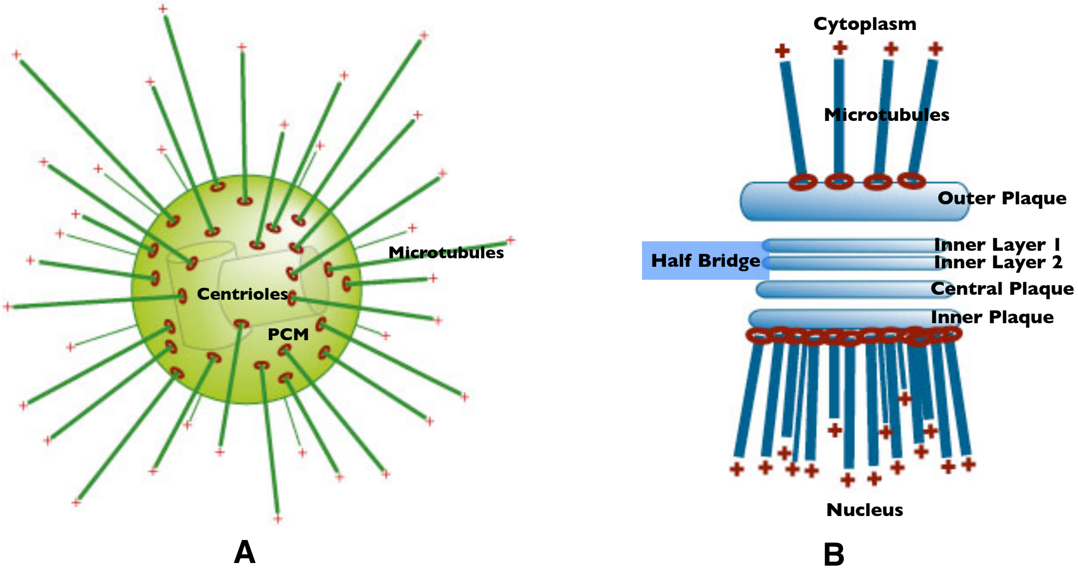

In fungi, the MTOC is called Spindle Pole Body (SPB) and it has an overall shape as seen in Figure 1B. The SPB can be described as a set of layers or plaques. The plaques are localized in, between and outside of the nuclear membrane. The outer plaque is in the cytoplasm, from which cytoplasmic MT emanate. Following is the first and second intermediate layer (IL1 and IL2) and the central plaque. The central plaque is associated with the Half Bridge of the nuclear envelope and it is the site of SPB biogenesis. The inner plaque faces the nucleus, from which nuclear MT emanate, and the third plaque which spans the nuclear membrane (Jaspersen and Winey 2004). Similarly to the concentric layers in the Centrosome, the SPB plaques contain different proteins with very distinct functions.

On Microtubules

A common feature that can be observed in the Centrosome and SPB representations in Figure 1, are MTs. MTs are comprised of αβ-Tubulin heterodimers (Fig. 2A) that are arranged into protofilaments that form a hollow polymer of 25nm in diameter (Fig 2C). αβ-Tubulin assemble in a GTP dependent manner and as they assemble in the MT, they can make 2 kinds of contacts. One contact is a longitudinal contact that is the length of the protofilament and the other contact is a lateral and symmetric contact between heterodimers (Fig. 2B) (Nogales, Wolf et al. 1998, Nogales, Whittaker et al. 1999).

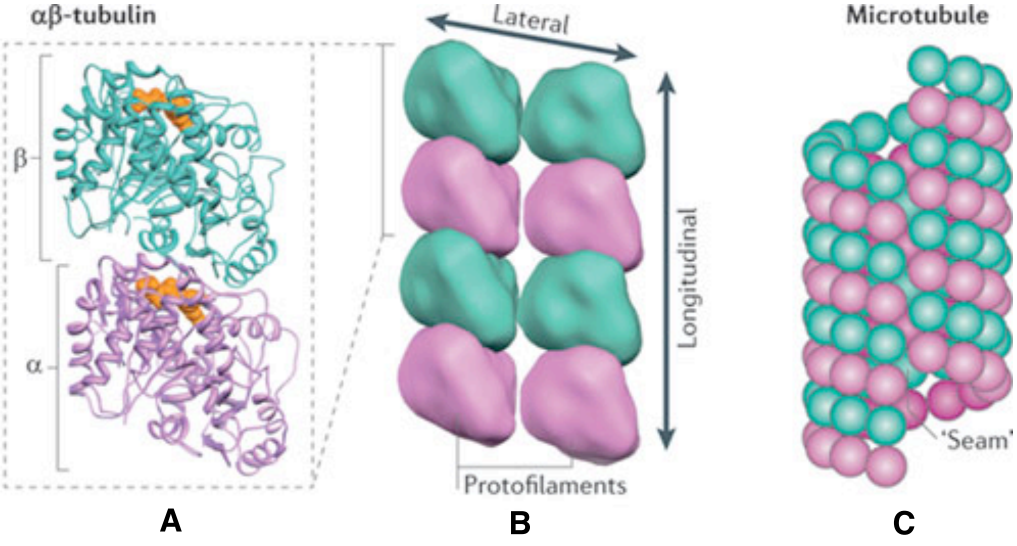

Figure 2: Structures of αβ-Tubulin dimers as: (A) Atomic model of αβ-Tubulin bound to GTP. (B) Contacts formed by αβ-Tubulin in a protofilament. Note the symmetry between heterodimers (C) αβ-Tubulin forming a MT. Figure adapted from **(Kollman, Merdes et al. 2011)**

While there are some exceptional cases (Chalfie and Thomson 1982), most MTs *in vivo* are 13-protofilaments (Ledbetter and Porter 1964, Tilney, Bryan et al. 1973, Evans, Mitchison et al. 1985) while the *in vitro* formed MTs can have between 11 and 16 protofilaments. It is thought that the 13-protofilament geometry allows for the protofilaments to run straight along the MT length, thus allowing motor proteins to remain on the same face of the structure.

Because αβ-Tubulin always assemble in the same directionality, MTs have a polarity; this is also used by motor proteins to transport cargo.

αβ-Tubulin can spontaneously nucleate into MTs. The initial step of MT nucleation *in vitro* is the formation of small assemblies. These small assemblies are not energetically favored, resulting in slow formation or growth (Figure 3); it is not until a larger assembly has formed that the formation of MT proceeds very rapidly (Rice, Montabana et al. 2008). *In vivo,* the cell overcomes this energy barrier by having MT nucleators; in this manner the cell can tightly control MT nucleation.

On Microtubule Nucleators

One of the proteins that are found on the PCM, the outer, and inner plaque is γ-Tubulin. γ-Tubulin is an essential protein in the cell and it is conserved in all eukaryotes; it belongs to the Tubulin superfamily and shares ~30% amino acid identity with αβ-Tubulin (Oakley and Akkari 1999).

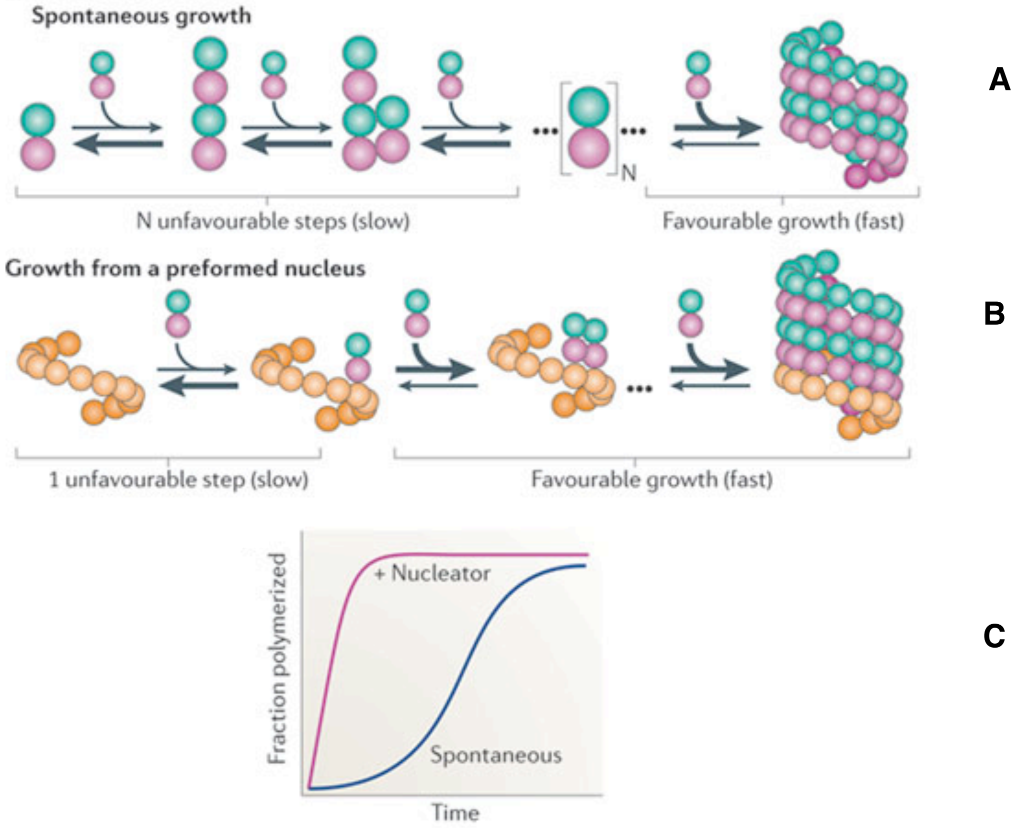

Figure 3: Microtubule growth (A) Growth steps in spontaneous nucleation. MT need a N sized small assembly to initiate a favorable growth. (B) Growth steps from a nucleator. In this case, favorable growth is achieved more efficiently. (C) Rate of polymerization given spontaneous nucleation vs. nucleation with a nucleator. Figure adapted from **(Kollman, Merdes et al. 2011)**

The role of γ-Tubulin in the cell is to nucleate MTs; like αβ-Tubulin, γ-Tubulin also binds to GTP. GTP binding is important for healthy MT nucleation and dynamics, but its mechanism of action is still unknown (Aldaz, Rice et al. 2005, Gombos, Neuner et al. 2013).

γ-Tubulin is found as part of a ~2.2MDa protein complex named γ-Tubulin Ring Complex or γTuRC. If treated with a high-salt concentration, γTuRC can dissociate into the γ-Tubulin Small Complex or γTuSC, a 300kDa complex where γ-Tubulin can be found. In essence, γTuRC are formed out of 7 repeats of γTuSC. Depending on the organism, γTuRCs can be formed from repeats of 3 to 9 different proteins (including γ-Tubulin). For example, γTuRCs in *S. cerevisiae* are repeats of 3 different proteins: γ-Tubulin, GCP2, and GCP3 (Rout and Kilmartin 1991, Kollman, Polka et al. 2010), while in *D. melanogaster* γTuRCs are formed of 8 different proteins: γ-Tubulin, GCP2, GCP3, GCP4, GCP5, GCP6, Mozart1 and GCPWD. *H. Sapiens* γTuRC have Mozart2, in addition to the same proteins as in the *D. melanogaster.* These proteins can be summarized in Table 1, for *S. cerevisiae* and *D. melanogaster.*

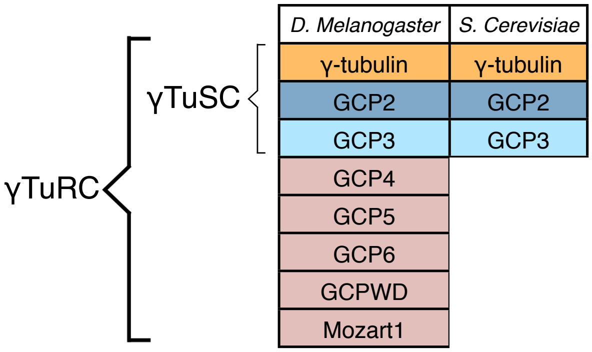

D. Melanogaster	*S. Cerevisiae*
γ-tubulin	γ-tubulin
GCP2	GCP2
GCP3	GCP3
GCP4	
GCP5	
GCP6	
GCPWD	
Mozart1	

Table 1: γTuRC components. *S. cerevisiae* and *D. melanogaster* share the basic subunits of γTuRC, which in turn for γTuSC. In addition, *D. melanogaster* has an additional 5 proteins.

The γTuRC component proteins GCP2-GCP6, contain 2 sequence motifs that are conserved across species. These motifs are called Grip1 and Grip2. They span ~100 and ~200 amino acids respectively and are thought to mediate protein-protein interaction among GCPs and among GCPs and γ-Tubulin (Fig. 4) (Gunawardane, Martin et al. 2000, Murphy, Preble et al. 2001, Guillet, Knibiehler et al. 2011).

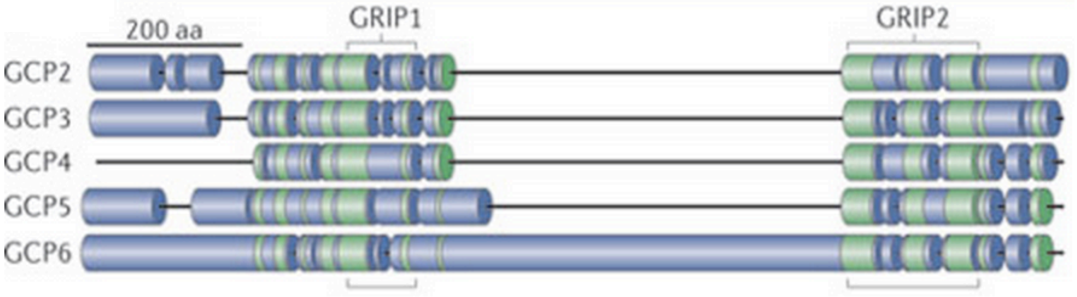

Figure 4: Sequence of the GCPs. GCPs contain 2 distinct motifs dubbed Grips 1 and 2. and the location in the protein sequence is maintained. Figures adapted from **(Kollman, Merdes et al. 2011)**

GCPWD and Mozart1/2 do not contain any Grip motifs, but they are thought to play a role in γTuRC localization and assembly. GCPWD interacts with the Augmin complex and it is thought to help target the γTuRC to the mitotic spindle (Uehara, Nozawa et al. 2009). Mozart1/2 are thought to help localize γTuRC to MTOCs and alter the arrangement of GCP3 to facilitate MT growth (Teixido-Travesa, Villen et al. 2010, Dhani, Goult et al. 2013, Masuda, Mori et al. 2013).

The overall structure of the γTuRC is conserved through species (Moritz, Braunfeld et al. 1995, Zheng, Wong et al. 1995, Kollman, Polka et al. 2010). The “ring” is formed by arranging 7 γTuSC (Fig. 5A) into a one start-helix (Fig. 5B). This arrangement allows the γTuRC to nucleate MT by acting as a “template” from which protofilaments can form (Fig. 5C). The arrangement is necessary for MT nucleation, because non-oligomerized γTuSC are not as potent MT nucleators as γTuRC (Oegema, Wiese et al. 1999) (Fig. 6).

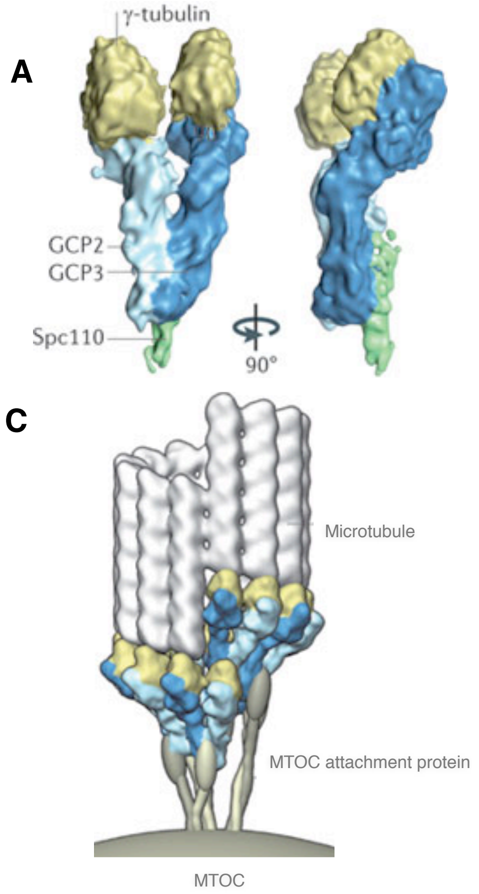

Figure 5: γTuSC and γTuRC structures in *S. cerevisiae* (A) γTuSC showing in dark blue GCP3, GPC2 in light blue, γ-Tubulin in golden. Even though Spc110 is not part of the core γTuSC components it mediates the oligomerization of γTuSC into γTuRC. Spc110 is depicted in green. (B) Top and side views of γTuRC. The 13-protofilament is evident thanks to the 1-start helix arrangements of the γTuSC. (C) Template model of the MT nucleation via γTuRC and its attachment to the MTOC via an attachment protein like Spc110. Figures adapted from **(Kollman, Merdes et al. 2011)**

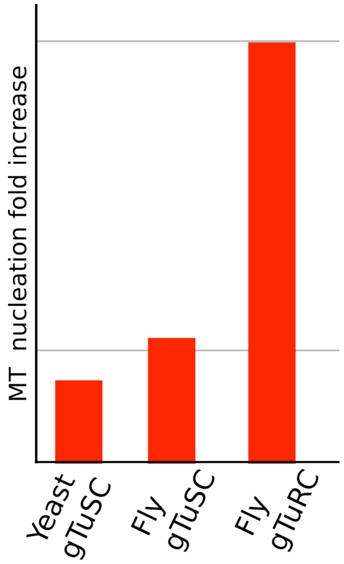

Figure 6: MT nucleation between complexes shows the fold increase between fly (*D. melanogaster)* γTuRC, γTuSC and yeast (*S. cerevisiae*) γTuSC. γTuRCs can nucleate MT ~ 7x more than γTuSC.

The overall architecture in Figure 5A observed in *S. cerevisiae*. γTuSCs purified in vitro can be assembled into γTuRC with the addition of Spc110 (Kollman, Zelter et al. 2008). In higher organisms, this architecture is thought to be very similar even though there is currently only a low-resolution EM structure of the *D. melanogaster* γTuRC(Moritz, Braunfeld et al. 2000).

The GCP4-6 are thought to be incorporated in the ring supplanting either GCP2 or GCP3 in some of the γTuSC. The structure of GCP4, GCP2, and GCP3 is conserved and so is their interaction with γ-Tubulin (Guillet, Knibiehler et al. 2011). Most likely, GCP2 and GCP6 share similar structures and are able to interact with γ-Tubulin. GCP4-6 are non-essential proteins but their absence causes some destabilization of γTuRC and mislocalization of γ-Tubulin, and while mitosis still progresses, it does with a higher mitotic index and gives rise to more abnormal spindles (Colombié, Vérollet et al. 2006, Xiong and Oakley 2009). Despite these "errors" most cells are able to continue through mitosis; this outcome is expected given that γTuRCs are able to form without GCP4-6 (Kollman, Polka et al. 2010).

In order to understand what role are these components doing in the complex and what relationship they have with MT nucleation, a higher eukaryote molecular view of the γTuRC is needed. The following chapters in this manuscript detail the work done to try to understand from a molecular stand point: How are these complexes arranged within the γTuSC and γTuRC? What is their stoichiometry? and what is the spatial relationship among them.

Bibliography

Aldaz, H., L. Rice, T. Stearns and D. Agard (2005). "Insights into microtubule nucleation from the crystal structure of human g-tubulin." Nature.

Bornens, M. (2002). "Centrosome composition and microtubule anchoring mechanisms." Curr Opin Cell Biol **14**(1): 25-34.

Bornens, M. (2012). "The centrosome in cells and organisms." Science **335**(6067): 422-426.

Chalfie, M. and J. N. Thomson (1982). "Structural and functional diversity in the neuronal microtubules of Caenorhabditis elegans." J Cell Biol **93**(1): 15-23.

Colombié, N., C. Vérollet, P. Sampaio, A. Moisand, C. Sunkel, H. M. Bourbon, M. Wright and B. Raynaud-Messina (2006). "The Drosophila gamma-tubulin small complex subunit Dgrip84 is required for structural and functional integrity of the spindle apparatus." Mol Biol Cell **17**(1): 272-282.

Dhani, D. K., B. T. Goult, G. M. George, D. T. Rogerson, D. A. Bitton, C. J. Miller, J. W. Schwabe and K. Tanaka (2013). "Mzt1/Tam4, a fission yeast MOZART1 homologue, is an essential component of the gamma-tubulin complex and directly interacts with GCP3Alp6." Mol Biol Cell **24**(21): 3337-3349.

Evans, L., T. Mitchison and M. Kirschner (1985). "Influence of the centrosome on the structure of nucleated microtubules." J Cell Biol **100**(4): 1185-1191.

Gombos, L., A. Neuner, M. Berynskyy, L. L. Fava, R. C. Wade, C. Sachse and E. Schiebel (2013). "GTP regulates the microtubule nucleation activity of gamma-tubulin." Nat Cell Biol **15**(11): 1317-1327.

Guillet, V., M. Knibiehler, L. Gregory-Pauron, M. H. Remy, C. Chemin, B. Raynaud-Messina, C. Bon, J. M. Kollman, D. A. Agard, A. Merdes and L. Mourey (2011). "Crystal structure of gamma-tubulin complex protein GCP4 provides insight into microtubule nucleation." Nat Struct Mol Biol **18**(8): 915-919.

Gunawardane, R. N., O. C. Martin, K. Cao, L. Zhang, K. Dej, A. Iwamatsu and Y. Zheng (2000). "Characterization and reconstitution of Drosophila gamma-tubulin ring complex subunits." The Journal of Cell Biology **151**(7): 1513-1524.

Ishikawa, H. and W. F. Marshall (2011). "Ciliogenesis: building the cell's antenna." Nat Rev Mol Cell Biol **12**(4): 222-234.

Jaspersen, S. and M. Winey (2004). "The budding yeast spindle pole body: structure, duplication, and function." Annu. Rev. Cell. Dev. Biol. **20**: 1-28.

Kollman, J. M., A. Merdes, L. Mourey and D. A. Agard (2011). "Microtubule nucleation by gamma-tubulin complexes." Nat Rev Mol Cell Biol **12**(11): 709-721.

Kollman, J. M., J. K. Polka, A. Zelter, T. N. Davis and D. A. Agard (2010). "Microtubule nucleating gamma-TuSC assembles structures with 13-fold microtubule-like symmetry." Nature **466**(7308): 879-882.

Kollman, J. M., A. Zelter, E. G. Muller, B. Fox, L. M. Rice, T. N. Davis and D. A. Agard (2008). "The structure of the gamma-tubulin small complex: implications of its architecture and flexibility for microtubule nucleation." Mol Biol Cell **19**(1): 207-215.

Ledbetter, M. C. and K. R. Porter (1964). "Morphology of Microtubules of Plant Cell." Science **144**(3620): 872-874.

Mahen, R. and A. R. Venkitaraman (2012). "Pattern formation in centrosome assembly." Curr Opin Cell Biol **24**(1): 14-23.

Masuda, H., R. Mori, M. Yukawa and T. Toda (2013). "Fission yeast MOZART1/Mzt1 is an essential gamma-tubulin complex component required for complex recruitment to the microtubule organizing center, but not its assembly." Mol Biol Cell **24**(18): 2894-2906.

Mennella, V., B. Keszthelyi, K. L. McDonald, B. Chhun, F. Kan, G. C. Rogers, B. Huang and D. A. Agard (2012). "Subdiffraction-resolution fluorescence microscopy reveals a domain of the centrosome critical for pericentriolar material organization." Nat Cell Biol **14**(11): 1159-1168.

Moritz, M., M. B. Braunfeld, V. Guénebaut, J. Heuser and D. A. Agard (2000). "Structure of the gamma-tubulin ring complex: a template for microtubule nucleation." Nat Cell Biol **2**(6): 365-370.

Moritz, M., M. B. Braunfeld, J. W. Sedat, B. Alberts and D. A. Agard (1995). "Microtubule nucleation by gamma-tubulin-containing rings in the centrosome." Nature **378**(6557): 638-640.

Murphy, S. M., A. M. Preble, U. K. Patel, K. L. O'Connell, D. P. Dias, M. Moritz, D. Agard, J. T. Stults and T. Stearns (2001). "GCP5 and GCP6: two new members of the human gamma-tubulin complex." Mol Biol Cell **12**(11): 3340-3352.

Nigg, E. A. and T. Stearns (2011). "The centrosome cycle: Centriole biogenesis, duplication and inherent asymmetries." Nat Cell Biol **13**(10): 1154-1160.

Nogales, E., M. Whittaker, R. A. Milligan and K. H. Downing (1999). "High-resolution model of the microtubule." Cell **96**(1): 79-88.

Nogales, E., S. G. Wolf and K. H. Downing (1998). "Structure of the alpha beta tubulin dimer by electron crystallography." Nature **391**(6663): 199-203.

Oakley, B. R. and Y. N. Akkari (1999). "Gamma-tubulin at ten: progress and prospects." Cell Struct Funct **24**(5): 365-372.

Oegema, K., C. Wiese, O. C. Martin, R. A. Milligan, A. Iwamatsu, T. J. Mitchison and Y. Zheng (1999). "Characterization of two related Drosophila gamma-tubulin complexes that differ in their ability to nucleate microtubules." The Journal of Cell Biology **144**(4): 721-733.

Rice, L. M., E. A. Montabana and D. A. Agard (2008). "The lattice as allosteric effector: structural studies of alphabeta- and gamma-tubulin clarify the role of GTP in microtubule assembly." Proc Natl Acad Sci USA **105**(14): 5378-5383.

Rout, M. P. and J. V. Kilmartin (1991). "Yeast spindle pole body components." Cold Spring Harb Symp Quant Biol **56**: 687-692.

Teixido-Travesa, N., J. Villen, C. Lacasa, M. T. Bertran, M. Archinti, S. P. Gygi, C. Caelles, J. Roig and J. Luders (2010). "The gammaTuRC revisited: a comparative analysis of interphase and mitotic human gammaTuRC redefines the set of core components and identifies the novel subunit GCP8." Mol Biol Cell **21**(22): 3963-3972.

Tilney, L. G., J. Bryan, D. J. Bush, K. Fujiwara, M. S. Mooseker, D. B. Murphy and D. H. Snyder (1973). "Microtubules: evidence for 13 protofilaments." J Cell Biol **59**(2 Pt 1): 267-275.

Uehara, R., R. S. Nozawa, A. Tomioka, S. Petry, R. D. Vale, C. Obuse and G. Goshima (2009). "The augmin complex plays a critical role in spindle microtubule generation for mitotic progression and cytokinesis in human cells." Proc Natl Acad Sci U S A **106**(17): 6998-7003.

Xiong, Y. and B. R. Oakley (2009). "In vivo analysis of the functions of gamma-tubulin-complex proteins." J Cell Sci **122**(Pt 22): 4218-4227.

Zheng, Y., M. L. Wong, B. Alberts and T. Mitchison (1995). "Nucleation of microtubule assembly by a gamma-tubulin-containing ring complex." Nature **378**(6557): 578-583.

Chapter II:

Localization and orientation of the γ-Tubulin Small Complex components using protein tags as labels for single particle EM

Abstract

γ-Tubulin Small Complex (γ-TuSC) is the universally-conserved complex in eukaryotes that contains the microtubule (MT) nucleating protein: γ-tubulin. γ-TuSC is a heterotetramer with two copies of γ-tubulin and one copy each of Spc98p and Spc97p. Previously, the structure of γ-TuSC was determined by single particle Electron Microscopy (EM) at 25 Å resolution. γ-TuSC is Y shaped with a single flexible arm that could be the key to regulating MT nucleation. EM gold labeling revealed the locations of γ-tubulin at the top of the Y. *In vivo* Fluorescence Resonance Energy Transfer (FRET) suggested the relative orientations of Spc98p and Spc97p but did not distinguish which large subunit formed the flexible arm. Here, using fluorescent proteins as covalently attached tags, we used class averages and 3D random conical tilt reconstructions to confirm the *in vivo* FRET results, clearly demonstrating that the Spc98p/97p C-termini interact directly with γ-tubulin. Most significantly we have determined that the flexible arm belongs to Spc98p and our data also suggests that the N-termini of Spc98p and Spc97p are crossed. More generally, our results confirm that despite their small size, covalently attached fluorescent proteins perform well as subunit labels in single particle EM.

Introduction

Microtubule Organizing Centers (MTOCs) organize the spatial and temporal patterns of microtubules by controlling their nucleation. Although the morphology of

MTOCs varies greatly among different phyla, all eukaryotes utilize γ-tubulin (Tub4p in yeast) to nucleate microtubules (Wiese and Zheng 2006). γ-tubulin is found in the 300 kDa γ-Tubulin Small Complex (γ-TuSC), a highly conserved heterotetramer with two copies of γ-tubulin and one each of Spc98p and Spc97p. In metazoa, γ-TuSC is a repeating component within the larger γ-Tubulin Ring Complex (γ-TuRC) (Moritz, Braunfeld et al. 2000). While both purified γ-tubulin and γ-TuRC are potent MT nucleators, nucleating activity for γ-TuSC is barely detectable even though it is the only γ-tubulin complex within the highly functional *S. cerevisiae* Spindle Pole Body (SPB) (Gunawardane, Martin et al. 2000, Vinh, Kern et al. 2002).

Recently, we determined the structure of the *S. cerevisiae* γ-TuSC at moderate resolution using single particle electron microscopy (Kollman, Zelter et al. 2008). The structure is Y-shaped and γ-tubulin is located in lobes at the tips of the two arms (Fig. 1A). One of the arms adopts different conformations due to a limited rotation about its base. Significantly, in all of the observed conformations, the γ-tubulins are held in nucleation incompatible orientations. We have suggested that this configuration may provide a way of regulating γ-TuSC activity, and that further movement of the flexibly attached arm is required to bring the two γ-tubulins together in a nucleation compatible orientation (Kollman, Zelter et al. 2008).

The location of γ-tubulin within γ-TuSC was determined by directly labeling His-tagged γ-tubulin with Ni-NTA nanogold. All attempts to label Spc98p and Spc97p in the same way using either 6x-His or 12x-His tags were unsuccessful due to very low labeling yields. Although the relative orientations of Spc98p and Spc97p were suggested by *in vivo* Fluorescence Resonance Energy Transfer (FRET) of dual-labeled complexes (Fig. 1B), these experiments were unable to distinguish Spc98p and Spc97p in the EM structure. Further, because the FRET experiments examined γ-TuSCs assembled at the SPB, there was the potential for confusing intra- and inter-complex FRET signals. Thus, we sought a more direct way to determine the locations and orientations of the γ-TuSC components.

Previous reports have shown the benefits of using small proteins as covalent labels for localization in EM. In several cases two-dimensional averages were used to localize tagged components. (Alcid and Jurica 2008, Bertin, McMurray et al. 2008, Jones, Meng et al. 2008, Li, Chavan et al. 2008). In at least two previous studies, reconstructions of tagged complexes yielded more precise three-dimensional localization (Kratz, Bottcher et al. 1999, Bueler and Rubinstein 2008). Adopting a similar approach**,** we generated γ-TuSC tagged at the N- or C- termini of Spc98p or Spc97p with yellow fluorescent protein (YFP) or cyan fluorescent protein (CFP). In three cases we were able to clearly identify tags, which were in a range of positions due to the flexibility of the linker. For both the N- and C-terminally tagged Spc97p, we could classify particles based on the position of the tag and generate random conical tilt reconstructions for each class. This allowed us to identify the positions of the termini of each protein. In addition, our data shows that 3-D reconstructions of tagged small complexes are feasible, despite the small size of the tag, and could be used as a general spatial localization method.

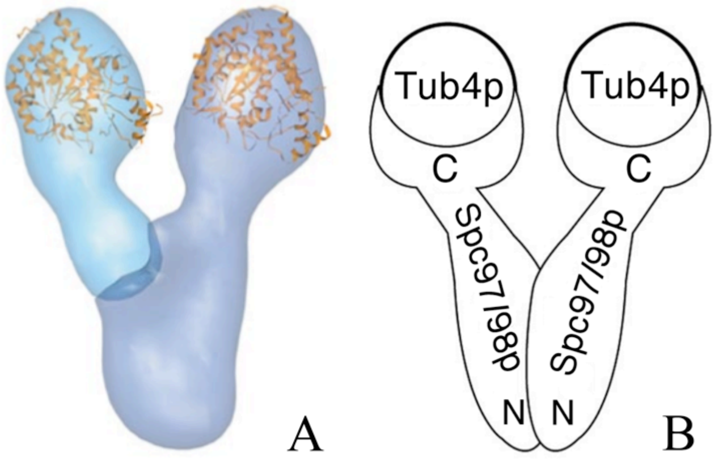

Figure 1:

A) Electron microscopy reconstruction of the *S. cereviseae* γ-TuSC. Light blue represents the flexibly attached arm and the more rigid body is presented in dark blue. The location of γ-tubulin was indicated by gold labeling, and the crystal structure of human γ-tubulin was manually fit into the structure (Kollman, Zelter et al. 2008). B) A schematic representation of the arrengement of γ-TuSC proteins based on the relative orientations of N- and C- termini determined by *in vivo* FRET.

Methods

The following γ-TuSC constructs were overexpressed in Sf9 cells and purified as previously described (Vinh, Kern et al. 2002): YFP tagged C-terminus of Spc97p (*γ-TuSC:Spc97pYFP*), YFP tagged N-terminus of Spc97p (*γ-TuSC:YFPSpc97p*), CFP tagged N-terminus of Spc98p (*γ-TuSC:CFPSpc98p*) and CFP tagged C-terminus of Spc98p *(γ-TuSC: Spc98pCFP)*. The linker connecting the fluorescent protein to the complex in each construct is 7 to 10 amino acids long. In each case, SDS-PAGE gels showed a band of the correct molecular weight for the tagged component (Fig. 2). The faint bands below the CFP-tagged constructs in the lanes *γ-TuSC:CFPSpc98p* and *γ-*

TuSC:Spc98pCFP, are thought to be a minor degree of degradation of the termini containing the tags. In the same lanes, the bands immediately above Tub4p are likely to be a protein contaminant, possibly a chaperone as TRiC-like particles are observed in the EM samples. To assure that this band is contamination and not a severe degradation product, we quantified the protein ratios between bands corresponding to the tagged and untagged Spc97p/98p and Tub4p in each SDS-PAGE lane (Figure 2) using ImageJ (Abramoff, Magelhaes et al. 2004). Significantly, the ratios to Tub4p corresponded to the expected stoichiometry of 2:1:1:1, indicating no significant degradation of the tagged proteins.

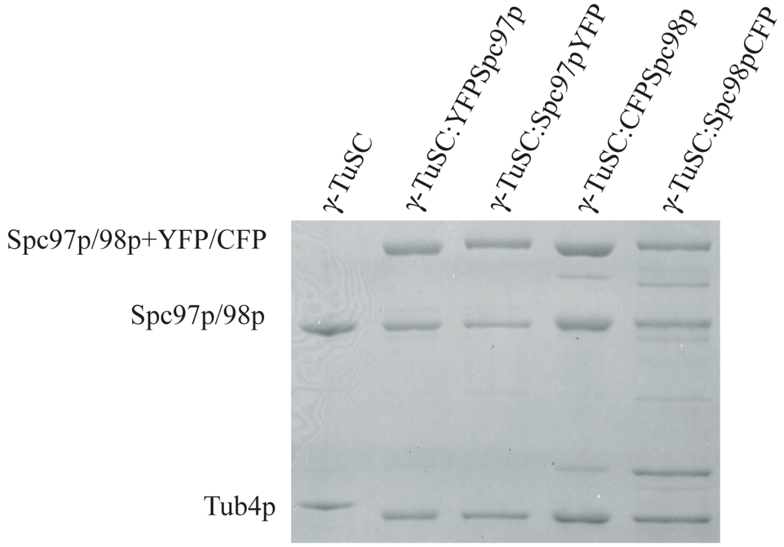

untagged Spc97p/98p:Tub4p	1.2	0.5	0.4	0.6	0.5
tagged Spc97p/98p:Tub4p	-	0.6	0.6	0.6	0.4

Figure 2: SDS-PAGE of γ-TuSC complexes. 1) γ-TuSC; 2) *γ-TuSC:YFPSpc97p*; 3) *γ-TuSC:Spc97pYFP*; 4) *γ-TuSC:CFPSpc98p* and 5) *γ-TuSC:Spc98pCFP.* The Tub4p His-tag linker is longer in the γ-TuSC, hence the Tub4p band migrates a bit slower than the other constructs. The band above Tub4p in the Spc98p-CFP constructs (Lanes 4,5) thought to be contamination, as it was observed on the

EM samples. In addition, the ratios (see below SDS-PAGE) between proteins in each lane corresponded to the γ-TuSC stoichiometry: 2:1:1:1, Tub4p, Spc97p/98p tagged and untagged.

Samples were prepared in thin layers of uranyl formate stain on carbon coated grids. Random Conical Tilt (RCT) data were acquired on a Tecnai T12 microscope (FEI Co., Netherlands) operating at 120kV and 52,000x magnification; images were recorded on a 4k×4k CCD camera (Gatan Inc., U.S) at a pixel size of 2.21 Å. The data were collected using the automated Conical Tilt feature of the UCSF Tomography package (Zheng, Kollman et al. 2007). The RCT data consisted of a 60° tilt image and three overlapping 0° images, allowing all particles observed at 60° to be used, maximizing data collection efficiency. Particle picking and image processing were done using WEB and SPIDER (Frank, Radermacher et al. 1996), respectively. For initial stages of processing, the particle images were binned 2×. On average the data sets for each construct contained 4800 particles. Reference-based alignment and classification of untilted particles was performed using the five classes of γ-TuSC (representing both movement of the flexible arm and slight differences in orientation relative to the grid) determined in our previous study (Kollman, Zelter et al. 2008). These class averages closely resembled the untagged references, and the fraction of particles in each class was similar for tagged and untagged complexes, indicating that the presence of the tag was not affecting the overall structure of the complex or how it interacted with the grid. Typically, the averages showed blurred density for the tag, indicating flexible attachment, most likely due to the length of the linker region. Principal Component Analysis (PCA) and hierarchical clustering were used to sort particles into classes with unique tag positions. These class averages were then used as references for a second round of alignment and classification. Euler angles were assigned to each tilted particle by combining the in-plane rotations determined during alignment with the data collection geometry. The unbinned tilted particles were back projected to form an initial model. Finally, three rounds of refinement were performed to correct the image shifts for each particle. EMAN (Ludtke, Baldwin et al. 1999) and Chimera (Pettersen, Goddard et al. 2004) were used to visualize the 2D images and the maps.

Results

For *γ-TuSC:YFPSpc97p* and *γ-TuSC:Spc97pYFP*, the extra 27 kDa mass of the tag was clearly visible in the raw micrographs and in both the 2-D class averages and the 3-D reconstructions (Figs. 3A-B and 3D-E). The tag appears as a small circle of density in the 2-D averages and as a droplet-shaped protruding density in the 3-D reconstructions. We manually docked the YFP crystal structure (PDB code: 1YFP) into the protruding density of the 3-D reconstruction of *γ-TuSC:Spc97pYFP* to show that they are comparable in size (Fig. 3I). We overlaid volumes from 3 or 4 of the classes for each of these constructs to show the different positions that the tag adopts (Fig. 3G-H).

In the case of *γ-TuSC:CFPSpc98p*, some of the tagged raw particles were visible in the raw micrographs (Fig. 3C) but in general, the tag seems to be much more flexibly attached, perhaps indicating inherent flexibility in the N-terminal region of Spc98p. Due to this disorder we were only able to obtain one 2-D average (Fig. 3F) with too few particles showing the tag in the same location for a reliable 3-D reconstruction. The variability manifests directly as more diffuse 2-D averages than those seen in Figs 3D and 3E. For *γ-TuSC:Spc98pCFP*, we were unable to locate the tag in the raw micrographs and in the 2-D class averages, possibly because the tag localizes on top or behind the complex.

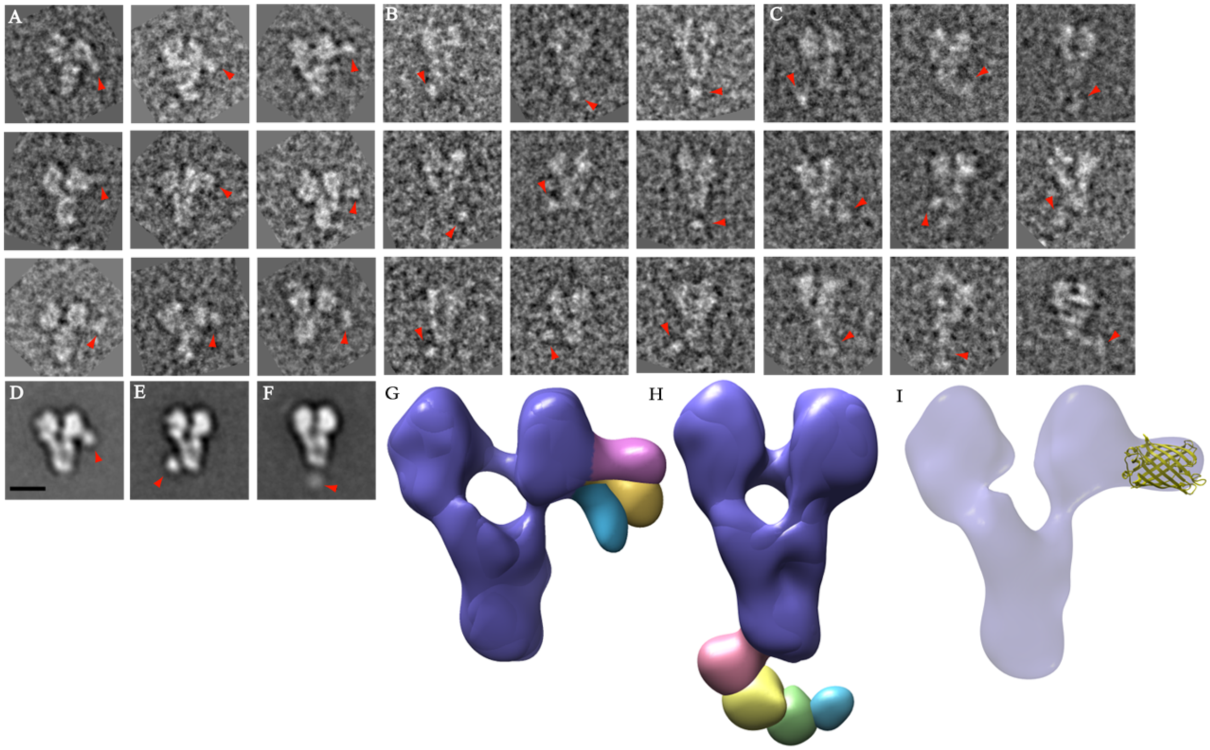

Figure 3: Structural analysis of tagged γ-TuSC complexes. A, B and C) Electron microscopy raw particles of *γ-TuSC:Spc97pYFP, γ-TuSC:YFPSpc97p* and *γ-TuSC:YFPSpc98p* respectively. The red arrow indicates the location of YFP and CFP density on each image. D, E and F) 2-D class averages of *γ-TuSC:Spc97YFPp, γ-TuSC:YFPSpc97p* and *γ-TuSC:CFPSpc98p* respectively with red arrows indicating the position of the tag. G and H) Overlay of the various 3-D reconstructions of *γ-TuSC:Spc97YFPp* and *γ-TuSC:YFPSpc97p*; the complex is shown in purple and the tags are colored red, blue, green and yellow.

I) 3-D reconstruction of *γ-TuSC:Spc97YFPp* with the crystal structure of YFP, shown in yellow, manually docked in the protruding density. Size bar is 10nm.

Discussion and Conclusions

Overall, our data confirm the locations of the N- and C- termini of Spc98p and Spc97p inferred from our previous *in vivo* FRET results (Kollman, Zelter et al. 2008) . In addition to confirming the Spc98p/97p subunit polarity, new structural features have been revealed. Importantly, we have shown that Spc97p forms the rigid arm of γ-TuSC, while Spc98p contains the flexible arm. Unexpectedly, the N- and C-terminal tags on Spc97p are on opposite sides of γ-TuSC. The tag at the N-terminus of Spc97p is more localized and favors a set of positions diagonally opposite to its C-terminus. We suggest that this indicates that the Spc97p and Spc98p are crossed, resulting in a crossed N-termini. Additionally, the N-terminal region of Spc98p appears to be inherently flexible, a finding consistent with sequence alignments of Spc97p and Spc98p which show Spc98p to have an additional ~150 amino acids at its N-terminus. In our previous study (Kollman, Zelter et al. 2008) we suggested that movement of the flexibly attached arm regulates γ-TuSC activity. Our 2-D averages and 3-D reconstructions clearly identify Spc98p as the subunit containing the flexible arm. The identification of the flexible subunit will help focus future studies involving mutagenesis and/or post-translational modifications on Spc98p to help understand the mechanism of regulation of MT nucleation by γ-TuSC.

Our data also confirms the termini localization indicated by our previous *in vivo* FRET study and further suggests that the N-termini are crossed. Together this allows us to update our model of γ-TuSC from the one seen in Fig 1B to the one in Fig. 4. Finally, our 2D averages and 3D reconstructions suggest that covalently-attached fluorescent protein tags are ideally suited to EM localization even at moderate resolutions.

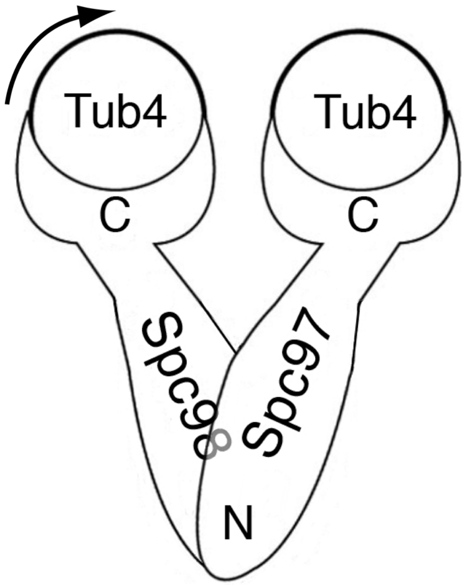

Figure 4: A revised model of the *S. cereviseae* γ-TuSC based on observed tag positions. The flexibility of Spc98p is indicated with an arrow, and the the N-termini of Spc97 and Spc98 are crossed.

Acknowledgments:

We are grateful to Shawn Zheng and Michael Braunfeld for assistance with electron microscopy. This work was supported by National Institutes of Health grants GM-31627 (to D.A.A. and R.M.C),R01GM-040506 and P41 RR-011823 (T.N.D and A. Z.) and the Howard Hughes Medical Institute.

Bibliography

Abramoff, M. D., P. J. Magelhaes and S. J. Ram (2004). "Image processing with ImageJ." Biophotonics International **11**(7): 36-42.

Alcid, E. A. and M. S. Jurica (2008). "A protein-based EM label for RNA identifies the location of exons in spliceosomes." Nat Struct Mol Biol **15**(2): 213-215.

Bertin, A., M. A. McMurray, P. Grob, S. S. Park, G. Garcia, I. Patanwala, H. L. Ng, T. Alber, J. Thorner and E. Nogales (2008). "Saccharomyces cerevisiae septins: supramolecular organization of heterooligomers and the mechanism of filament assembly." Proc Natl Acad Sci USA **105**(24): 8274-8279.

Bueler, S. A. and J. L. Rubinstein (2008). "Location of subunit d in the peripheral stalk of the ATP synthase from Saccharomyces cerevisiae." Biochemistry **47**(45): 11804-11810.

Frank, J., M. Radermacher, P. Penczek, J. Zhu, Y. Li, M. Ladjadj and A. Leith (1996). "SPIDER and WEB: processing and visualization of images in 3D electron microscopy and related fields." Journal of Structural Biology **116**(1): 190-199.

Gunawardane, R. N., O. C. Martin, K. Cao, L. Zhang, K. Dej, A. Iwamatsu and Y. Zheng (2000). "Characterization and reconstitution of Drosophila gamma-tubulin ring complex subunits." The Journal of Cell Biology **151**(7): 1513-1524.

Jones, P. P., X. Meng, B. Xiao, S. Cai, J. Bolstad, T. Wagenknecht, Z. Liu and S. R. Chen (2008). "Localization of PKA phosphorylation site, Ser(2030), in the three-dimensional structure of cardiac ryanodine receptor." Biochem J **410**(2): 261-270.

Kollman, J. M., A. Zelter, E. G. Muller, B. Fox, L. M. Rice, T. N. Davis and D. A. Agard (2008). "The structure of the gamma-tubulin small complex: implications of its architecture and flexibility for microtubule nucleation." Mol Biol Cell **19**(1): 207-215.

Kratz, P. A., B. Bottcher and M. Nassal (1999). "Native display of complete foreign protein domains on the surface of hepatitis B virus capsids." Proc Natl Acad Sci U S A **96**(5): 1915-1920.

Li, H., M. Chavan, H. Schindelin, W. J. Lennarz and H. Li (2008). "Structure of the oligosaccharyl transferase complex at 12 A resolution." Structure **16**(3): 432-440.

Ludtke, S. J., P. R. Baldwin and W. Chiu (1999). "EMAN: semiautomated software for high-resolution single-particle reconstructions." J Struct Biol **128**(1): 82-97.

Moritz, M., M. B. Braunfeld, V. Guénebaut, J. Heuser and D. A. Agard (2000). "Structure of the gamma-tubulin ring complex: a template for microtubule nucleation." Nat Cell Biol **2**(6): 365-370.

Pettersen, E. F., T. D. Goddard, C. C. Huang, G. S. Couch, D. M. Greenblatt, E. C. Meng and T. E. Ferrin (2004). "UCSF Chimera--a visualization system for exploratory research and analysis." J Comput Chem **25**(13): 1605-1612.

Vinh, D. B., J. W. Kern, W. O. Hancock, J. Howard and T. N. Davis (2002). "Reconstitution and characterization of budding yeast gamma-tubulin complex." Mol Biol Cell **13**(4): 1144-1157.

Wiese, C. and Y. Zheng (2006). "Microtubule nucleation: gamma-tubulin and beyond." Journal of Cell Science **119**(Pt 20): 4143-4153.

Zheng, S. Q., J. M. Kollman, M. B. Braunfeld, J. W. Sedat and D. A. Agard (2007). "Automated acquisition of electron microscopic random conical tilt sets." J Struct Biol **157**(1): 148-155.

Chapter III:

Structure of the γ-Tubulin Ring Complex in D. melanogaster

Preface

The following work would not have been possible without Michelle Moritz's guidance throughout the preparation of *D. melanogaster* embryo extracts, gradients and understanding and working with a big *D. melanogaster* population. Also, the progress on the native γTuRC population would have never been possible without Sandra Rodriguez and Flora Kan, who are excellent fly keepers.

Tony Shermoen from the O'Farrell lab graciously helped on planning *D. melanogaster* crosses and supplied the balancer *D. melanogaster* necessary to carry the project to fruition.

The baculovirus part of this project was done along with Mariano Tabios, who had graciously cloned most of the γTuRC genes into a baculovirus system. Mariano also guided me throughout insect cell culture and baculovirus production.

The cryo-EM and cryo-EMT would not have been possible without the patience and guidance of Sam Li, who taught me how to collect and process cryo-EMT data, in addition to loading and unloading grids in the microscopes. Michael Braunfeld and Agustin Avila-Sakar were also key on teaching me how to do single-particle cryo-EM.

Introduction

The following chapter represents the work done in obtaining a structure of the *D. melanogaster* γ-Tubulin Ring Complex (γTuRC).

From previous work done in the lab (Moritz, Braunfeld et al. 2000), it was known that the γTuRC presented the following 2 challenges for a high-resolution structural work: 1) The protein complex yields from the current prep were too low and 2) The purified complex seemed heterogeneous. The γTuRC protocol is a native pulldown from 3-4h *D. melanogaster* embryos (See Methods section). γTuRCs are pulled down with a peptide antibody raised against ~16 C-terminal aminoacids of either γ-Tubulin, GCP2 or GCP3. The heterogeneity observed on the γTuRC was thought to be due to the steric effects of the antibody binding, the complex falling apart, and/or different conformational states that would regulate MT nucleation by γTuRC. While the first 2 could be overcome by improving the current prep, the latter made EM the choice for structural work. In addition, the low yield was attributed to a high affinity binding to the antibody given that approximately half of the material would be bound to the column and not elute.

In order to overcome yield and antibody induced distortions, a new approach for the γTuRC protocol had to be established. In total, 3 approaches were tried. The first one was generating a mutant *D. melanogaster* that would carry a copy of one of the GCP with a Tandem Affinity Purification (TAP) system. The second approach was to overexpress γTuRC in a baculovirus system and adding a TAP system to some of the components. The last approach was to generate new peptide antibodies against GCP4-6 and test if the elution in the γTuRC native pull down was more efficient.

The last approach proved to be the successful one. While this approach does not permit a more in depth biochemical analysis of the complex components, the quantities obtained allowed for measuring stoichiometry using SDS-PAGE and Mass-

Spectrometry. The Mass-spectrometry was done by Yi Shi, from the Chait Lab in Rockefeller University.

The chapter is divided into 5 sections. The first 3 sections explain the results from the improvement of the γTuRC protocol and the γTuRC structure, the 4th section explains the stoichiometry and the last section has the Methods for all the work done in this chapter.

Section 1: TAP GCP2 and GCP4 *D. melanogaster*

The constructs generated were: 6xHis-GCP2-Strep•II (GCP2-mt) and 6xHis-GCP4-Strep•II (GCP4-mt). Both constructs were included in a PhiC31 integration system in flies from the Bloomington Stock #24483. Flies were crossed until a hemizygous population was achieved (see Methods for a map of the crossings). After the crosses were achieved, the Strep•II had a point mutation that rendered the tag useless for detection and pulldown, so the focus was to use α6xHis and αGCP2 for detection and the GCP4, for lack of αGCP4 was set aside.

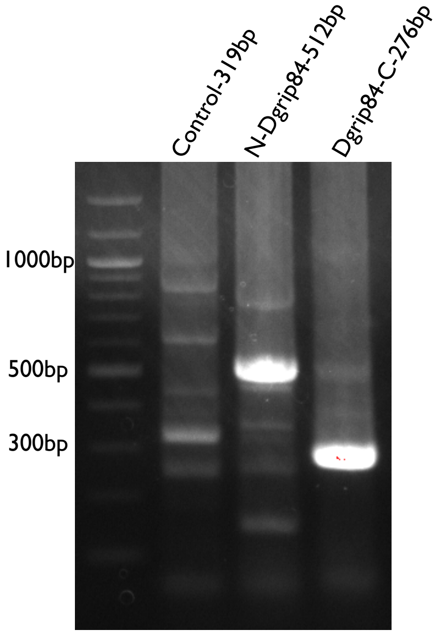

Figure 1: Genomic PCR of GCP2-mt. From left to right: Lane 1 is the DNA ladder, Lane 2 is the control primer whose

product is 319bp. Lane 3 is the N-terminal of GCP2 (or Dgrip84) primer whose product is 512bp and Lane 4 is the C-terminal of GCP2 primer whose product is 276bp.

For the hemizygous population, a genomic PCR on the N and C-terminal of the GCP2-mt, revealed that the gene was inserted (Fig. 1).

To assess GCP2-mt production, 3hr mutant and wild type (wt) *D. melanogaster* embryos were made into an extract and then clarified into a high-speed supernatant. A Western Blot of α6xHis was done on the wt and GCP2-mt extract (Fig. 2). The Western Blot results were ambiguous since the wt (Control) has a band similar to the GCP2-mt.

Given the ambiguity of the Western Blot, a small scale γTuRC prep was done to determine GCP2-mt production and inclusion in the complex. These results show that no γTuRC containing GCP2-mt was binding to the beads.

While the gene was inserted, it was unclear whether GCP2-mt was being expressed. What was very clear was that it was not getting included in the γTuRC, therefore another approach to improve yield and quality of γTuRC was taken.

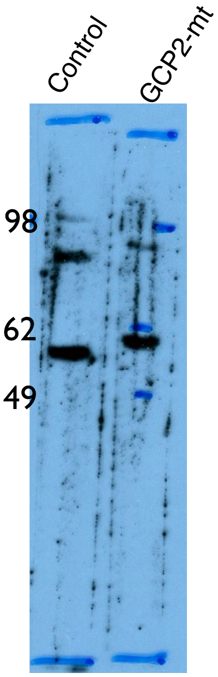

Figure 2: Western blot of high-speed *D. melanogaster* embryo extract. From left to right: Lane 1 is the control or wt extract and Lane 2 is the GCP2-mt extract. Numbers mark the molecular weight of the neighboring bands.

As a future direction, it might be necessary not to include a copy of the gene, but to replace it. While GCP2 is an essential protein, replacing GCP4-GCP6 might yield a positive result.

Section 2: Baculovirus expression of *D. melanogaster γTuRC*

As part of an ongoing effort in the lab to determine structures of various components of the γTuRC in *D. melanogaster* and *S. cerevisiae*, all GCP2-5 had been already been placed in the pFastBac baculovirus system from Invitrogen. As part of the γTuRC protocol improvement, GCP6 and γ-Tubulin for *D. melanogaster* were also included in the pFastBac system. All GCPs and γ-Tubulin were included in the with a TAP system, Table 1 shows the different constructs that were made.

Protein	***N-tag***	***C-tag***
γ-Tubulin	FLAG	--
GCP-WD	6xHis	--
GCP4	6xHis	--
GCP2	--	--
GCP2	6xHis	--
GCP3	--	--
GCP3	6xHis	--
GCP5	6xHis	--
GCP6	6xHis	Strep•II

Table 1: Baculovirus constructs for *D. melanogaster* γTuRC. Constructs were made with a variety of tags in the N- and C-terminal. Constructs that did not have a tag in one of their terminal, is denoted with --.

All virus were titered and added to Sf9, Sf21 and Hi5 cells with an MOI = 3. This MOI was chosen because it was the MOI where there was a strong expression of γ-Tubulin without a strong appearance of the chaperone TRiC.

Time points of baculovirus infected cells were taken of 20 and 40h post infection to assess expression of the components. When probed using Western Blot, it was clear that the individual components were expressed (as seen in Fig. 3) and that the expression was stronger after 40h post infection. In addition, α6xHis and αStrep•II were probed. α6xHis shows a clear expression of the components at 40h post infection.

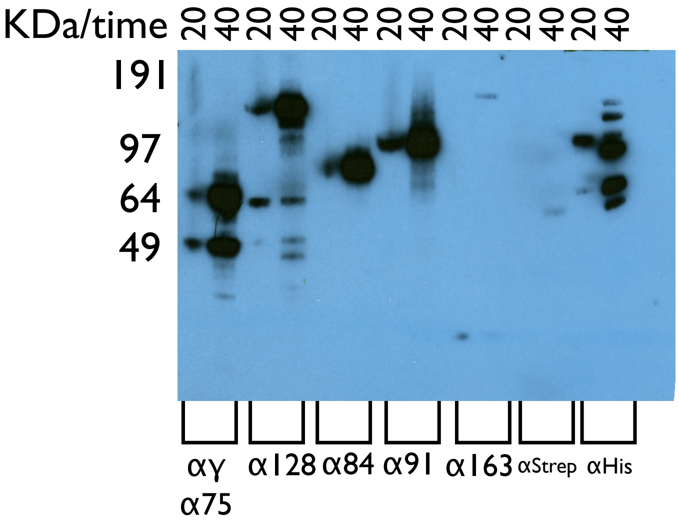

Figure 3: Western Blot of the γTuRC components. Lanes from left to right: Lane 1 and 2: αγTub and αGCP4 (α75) blots at 20 and 40h, respectively. Lane 3 and 4: αGCP5 (α128) blot at 20 and 40h, respectively. Lane 5 and 6 αGCP2 (α84) blot at 20 and 40h, respectively. Lane 7 and 8: αGCP3 (α91)

blot at 20 and 40h, respectively. Lane 9 and 10: αGCP6 (α163) blot at 20 and 40h, respectively. The last four lanes show αStrep•II and αHis for 20 and 40h.

While all GCPs (with the exception of GCP-WD and Mozart1, for lack of antibodies) and γ-Tubulin were shown to be expressing, protein preps from baculovirus infected cells did not show a strong or similar γTuRC pattern (Fig. 4A) as seen in γTuRC preps from *D. melanogaster* embryos (Fig. 4B). The preps were a two column preps (See Methods section) where the first column was a Ni-NTA followed by a Strep-Tactin column in order to capture γTuRCs that had GCP6, in essence the most complete γTuRCs. Furthermore, elution fractions were used to prepare negative-stain Electron Microscopy (EM) samples. In no fraction prepared, γTuRCs were observed that resembled γTuRC from *D. melanogaster* embryo preps (data not shown).

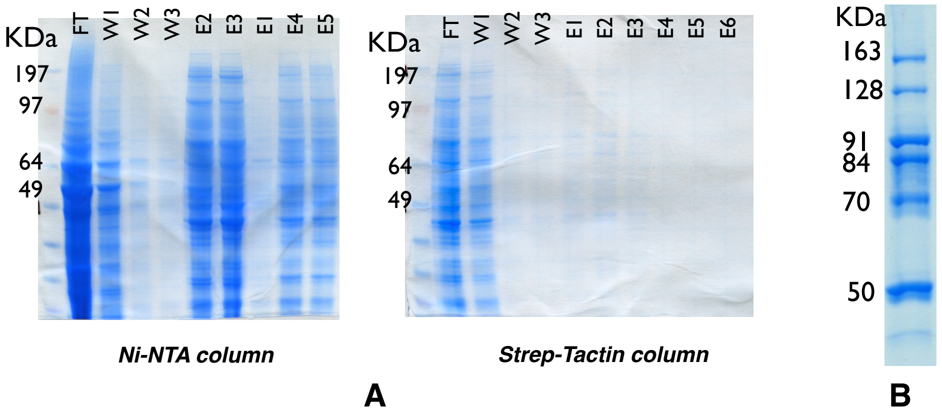

Figure 4: SDS-PAGE of γTuRC preps. (A) 2 column profile of a γTuRC prep from cells infected with baculovirus. Ni-NTA column is the first step and it shows from left to right, all the steps from Flow-through (FT), Wash1 (W!), Wash2 (W2), Wash3 (W3), Elution1 to Elution 5 (E1-E5). Similarly, the second column

is a Strep-Tactin column and it has the same nomenclature. (B) γTuRC prep from *D. melanogaster* embryos.

In addition, Elution #2 from the Strep-tactin column was run in a sucrose gradient (see Methods) to determine whether γTuRC was forming at the correct size. Embryo extract from *D. melanogaster* was run as a control. Figure 5 shows both the ponceau S stain (A) and the Western Blots for both gradients, blotting for γ-Tubulin, GCP4 (Dgrip75) and GCP5 (Dgrip128) (B) and (C) blotting for GCP3 (Dgrip91). In the control gradient, γ-Tubulin, GCP4, GCP3 and GCP5 can be readily seen in fraction #14, while in the Elution #2, GCP5 is mostly located in fractions 9-16, GCP4 and γ-Tubulin in 2-16 and lastly, GCP3 is located in fractions 6-8. This is indicative that γTuRC was not being formed as expected. It is possible that γ-Tubulin and the GCPs were forming subcomplexes or precursor γTuRC. Unfortunately, there was not a homogeneous population suitable for structural studies.

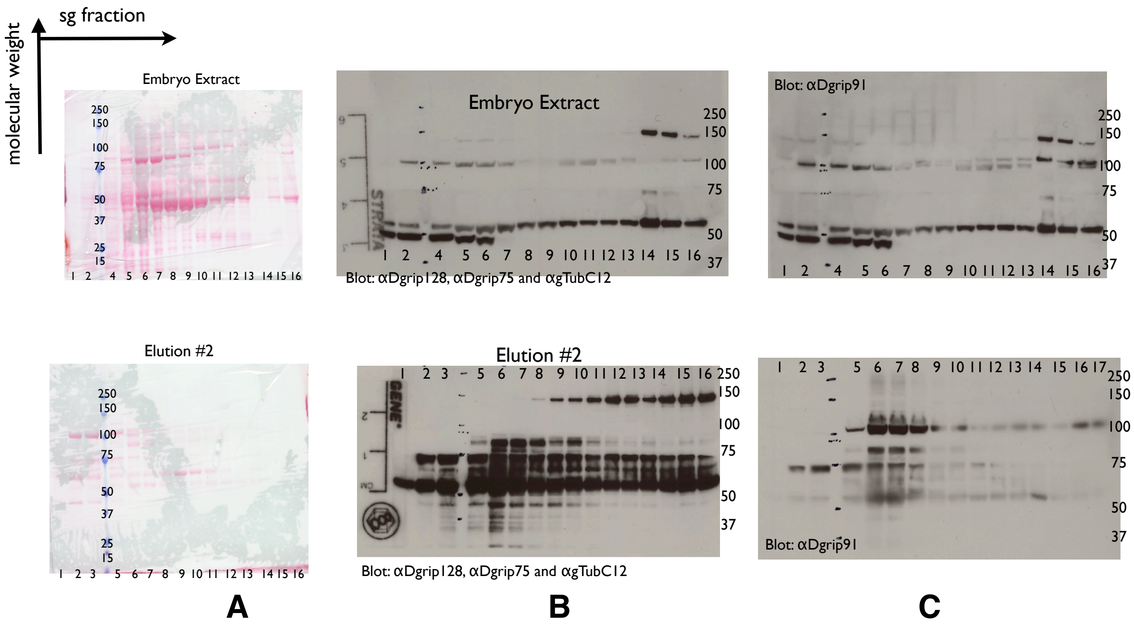

Figure 5: Sucrose gradients and ponceau S stains of γTuRC. Top row is the *D. melanogaster* embryo extract. Bottom row is the Elution #2 of the Strep-Tactin column of the baculovirus infected cells. Molecular weight is the latitude and the longitude is the sucrose gradient fraction, which is also the Stoke's radius of the molecule from small to big. (A) shows the ponceau S stain of both gradients. (B) Blots against γ-Tubulin, GCP4 and GCP5. (C) Blot against GCP3.

Section 3: Improvement in the purification and structure of the *D. melanogaster* γTuRC

Improving γTuRC yields from *D. melanogaster* embryo preps required 2 steps: the first step was to improve the elution of the complex from the antibody, because the current antibodies were not eluting. The second step was to increase the yield of complex.

To improve the elution, new antibodies were generated. Peptide antibodies were generated for GCP4, GCP5 and GCP6 against the last 16 C-terminal amino acids. These antibodies were purified (see Methods) and tested in γTuRC preps. Of the 3 antibodies, αGCP5 was the antibody that eluted γTuRC.

While this was an improvement on the elution, complex yields were not sufficient for cryo-Electron Microscopy (cryo-EM) structural studies. Several variations on the protocol were tried to improve yield: 1) magnetic beads 2) magnetic beads with a smaller elution volume, 3) glycerol on the elution buffer, 4) shorter elution times, and 5) scaling up the starting material. The amount and quality of γTuRC from variations 1, 2, 3 and 4, were all qualitative; and while they seemed to improve the elution, only 5 produced the most dramatic effect. Scaling up the protocol was done only on the starting material, the volumes for the elution and the washes were set to remain the same. The standard γTuRC protocol went from using a starting material of ~28mL (~21g) of 1:1 *D. melanogaster* embryo extract to 116mLs (~87g). The results of negative stained EM of the Elution fractions of the protocols can be readily seen in Figure 6. The quantity of γTuRC was enough for the preparation cryo-EM grids (Fig. 6C). Estimation of the concentration of complex from preps this size is ~40nM of γTuRC, while previously it could not be measured.

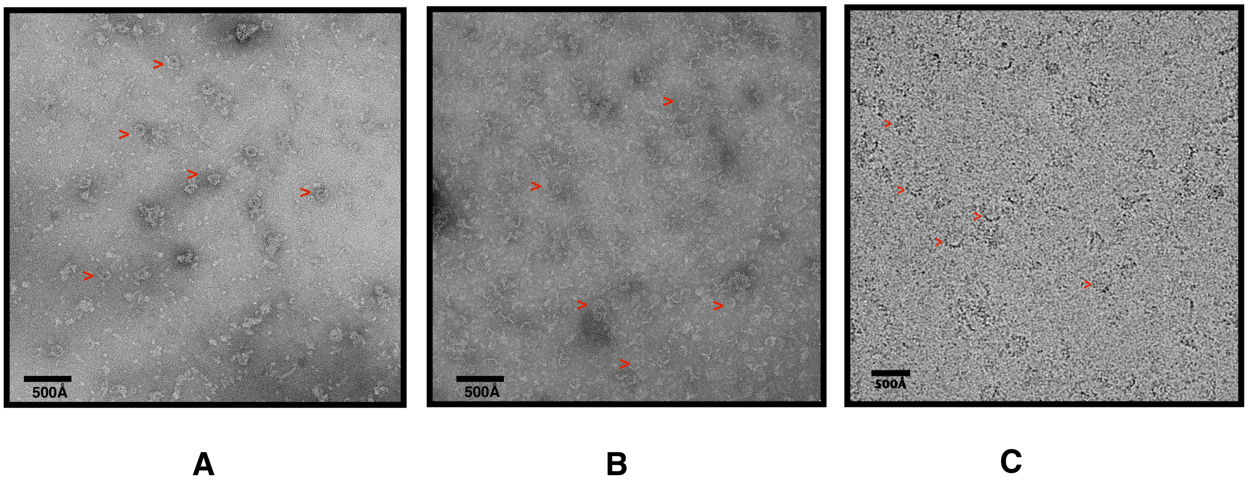

Figure 6: Standard and scaled γTuRC preps. γTuRCs are pointed with red arrows. (A) γTuRC prep with a starting material of 28mL (~21g) (B) γTuRC prep with a starting material of ~116mL (~87g) (C) Same as (B) but a cryo-EM sample. Size bar=500Å.

Initial structures of the γTuRC were done as a single-particle EM reconstructions using the *S. cerevisiae* γTuRC (Kollman, Polka et al. 2010) as an initial model. A total of

916 micrographs with a pixel size of 2.64Å/pix and a dose of ~28e^-/Å were used; the total number of particles used was 29780. Data was collected in an FEI F20 operating at 200kV, and equipped with an 8Kx8K CMOS detector from TVIPS. The micrographs were CTF corrected using our in-house CTF correction software called FocusRamp. Particle picking was done manually in EMAN1 (Ludtke, Baldwin et al. 1999). Projection matching was done using Xmipp2.4 (Sorzano, Marabini et al. 2004). After several rounds of refinement, the initial structure, as seen in Figure 7A showed heterogeneity in the direction of the Z axis. This indicated that the particles had an orientation preference on the grid. While the structure was distorted, features that differ from the *S. cerevisiae* γTuRC started appearing, giving an indication of the incorporation of the GCP4-6 into the ring.

To overcome a preferred orientation on the grid, an initial cryo-EM tomography data set was collected in the same microscope as before, using UCSF tomo (Zheng, Braunfeld et al. 2004). A total dose of ~70e^-/$Å^2$ was used and the tilt range was from -46° to 46° in 2° increments. The pixel size was 3.14Å/pix with a defocus of ~10µm. From the data collection session, 5 tomography sets were used for the reconstruction from which 99 subvolumes were extracted. Prior to reconstruction, the alignment was performed using colloidal gold beads as fiducial markers in IMOD (Kremer, Mastronarde et al. 1996). The data sets were CTF corrected (Fernandez, Li et al. 2006, Heymann and Belnap 2007) and reconstructed using Priism (Chen, Hughes et al. 1996). Subvolumes were extracted from the reconstructed data sets using IMOD. Subvolume averaging was done in Xmipp2.4 using the *S. cerevisiae* γTuRC as an initial model. In addition, a reference-free subvolume averaging was done to prevent any model bias. The results were similar. Figure 7B shows the reconstruction at ~50Å resolution.

While the resolution was low, features previously observed were present. The features are highlighted in yellow and orange. Figure 7C shows the *S. cerevisiae* γTuRC as a comparison between both γTuRC structures in 7A and 7B.

In order to increase the resolution, the subsequent data collection was done in a FEI F30, operating at 300kV and equipped with a K2 summit Direct Electron Detector. Data was collected using the One-Sweep method and Dose Fractionation implemented in UCSF tomo (See Chapter IV).

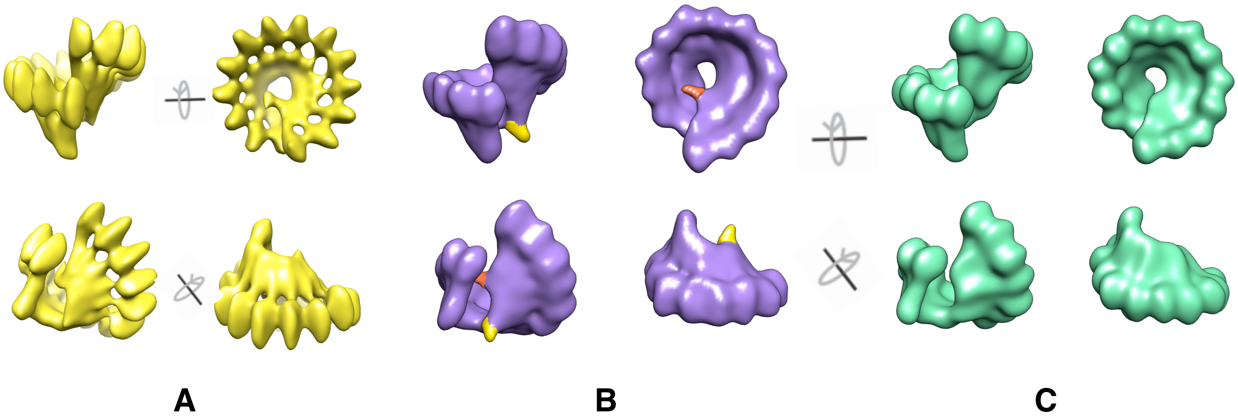

Figure 7: Initial structures of the *D. melanogaster* γTuRC. (A) Single-particle reconstruction of the γTuRC. γ-Tubulins denote the anisotropy in the structure, if compared with (C). (B) Subvolume average of γTuRC. The structure has a better angular distribution, and highlighted in orange and yellow are the extra densities. (C) *S. cerevisiae* γTuRC at 50Å resolution. Highlighted densities in (B) are not present.

A total dose of ~60e^{-}/Å^{2} was used and the tilt range was from -30° to 60° in 2° increments. The pixel size was 4.29Å/pix with a defocus range of 3.7-5.3µm.

The tomographic sets were aligned based on the Li et al,. (2013) (Li, Mooney et al. 2013) algorithm, but implemented for tomography data sets (See Chapter IV).

From the data collected, 42/55 tomography sets were used and were reconstructed as before. A final 1120 subvolumes were extracted and after manually reviewing the subvolumes, 1068 were kept for the final reconstruction. Similarly to the previous data set, all subvolume processing was done in Xmipp2.4 using the *S. cerevisiae* γTuRC as an initial model. In addition, a reference-free subvolume averaging was done to ensure that there was not any model bias; the results were similar.

The particles used for the reconstruction were 2x binned for a final pixel size of 8.58Å/pix. The reconstruction can be seen in Figure 8A, low-pass filtered to 45Å. The resolution of the reconstruction is ~34Å in the FSC=0.5 criterion, and ~32Å in the FSC=0.143 criterion. From the reconstruction, it can be seen that the particles still have anisotropy in the Z direction consistent with having a preferred orientation on the grid. Despite this anomaly, the extra densities can still be seen. The extra densities are highlighted in yellow and orange. For comparison, a structure of the *S. cerevisiae* γTuRC was low-pass filtered to 45Å (Fig. 8B).

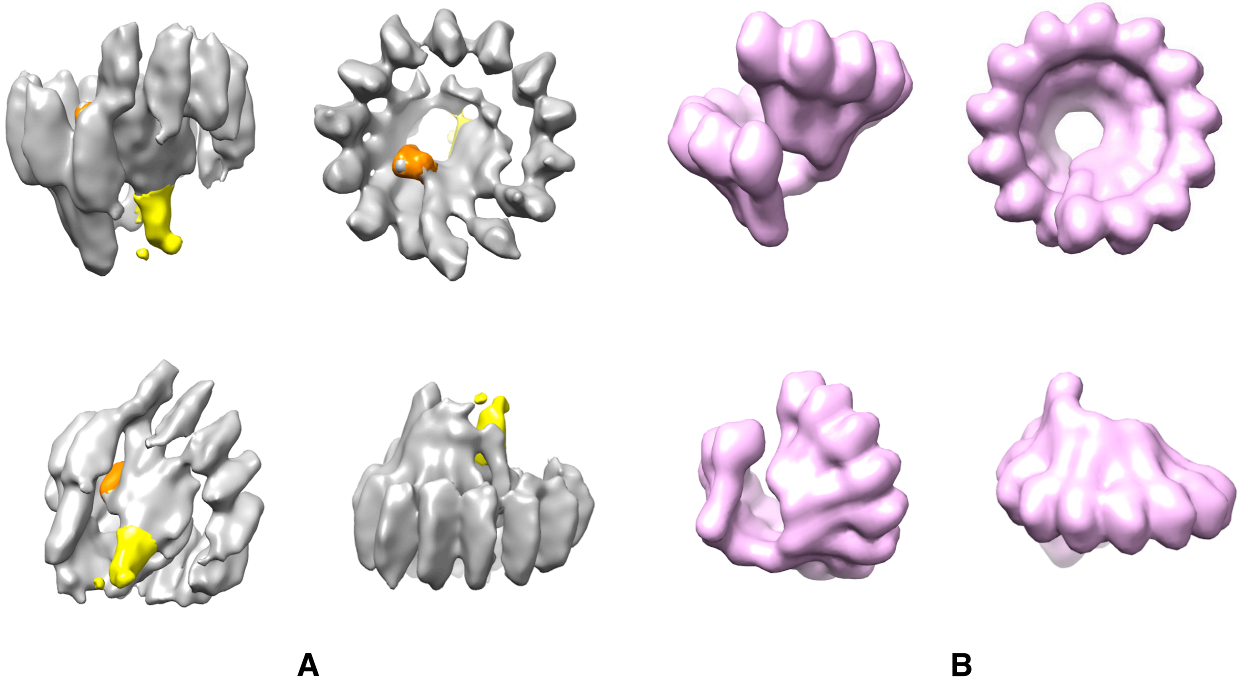

Figure 8: Structure of the *D. melanogaster* γTuRC. (A) Subvolume average of γTuRC. The structure is anisotropic due to poor angle distribution in the particle set. The resolution is ~34Å at the FSC=0.5 criterion. It has been low-pass filtered to 45Å (B) *S. cerevisiae* γTuRC at 45Å resolution. Highlighted densities in (A) are not present.

The top down view of the γTuRC in Figure 8A shows a region of missing density between γ-Tubulin and the GCPs. This region of missing density is indicative of 2 possibilities: 1) misalignment of the particles or 2) the existence of broken complex within the data set. The existence of broken complex can be seen in the negative-stain EM data; while γTuRCs appear intact, there is always a fraction that is broken. It was unclear if the γTuRC breaks due to interaction with the grid or it falls apart during the prep. In order to determine whether the reconstruction had broken γTuRCs in it, the data set was classified into 3 sets (Fig. 9). The results are quite striking, the highest populated class (55.7% of particles, Fig. 9B) appear to be partial γTuRC. The second highest populated class (44% of particles, Fig. 9C) which γTuRC appear to be similar to the structure obtained in Fig. 8 (Fig. 9A); it still has missing density between γ-Tubulin and the GCPs, indicating that there are either more broken complex in that class or that there is misalignment. Further classification in each, the first and second most populated classes is being carried on to determine what other species of particles are being included in these class-averages.

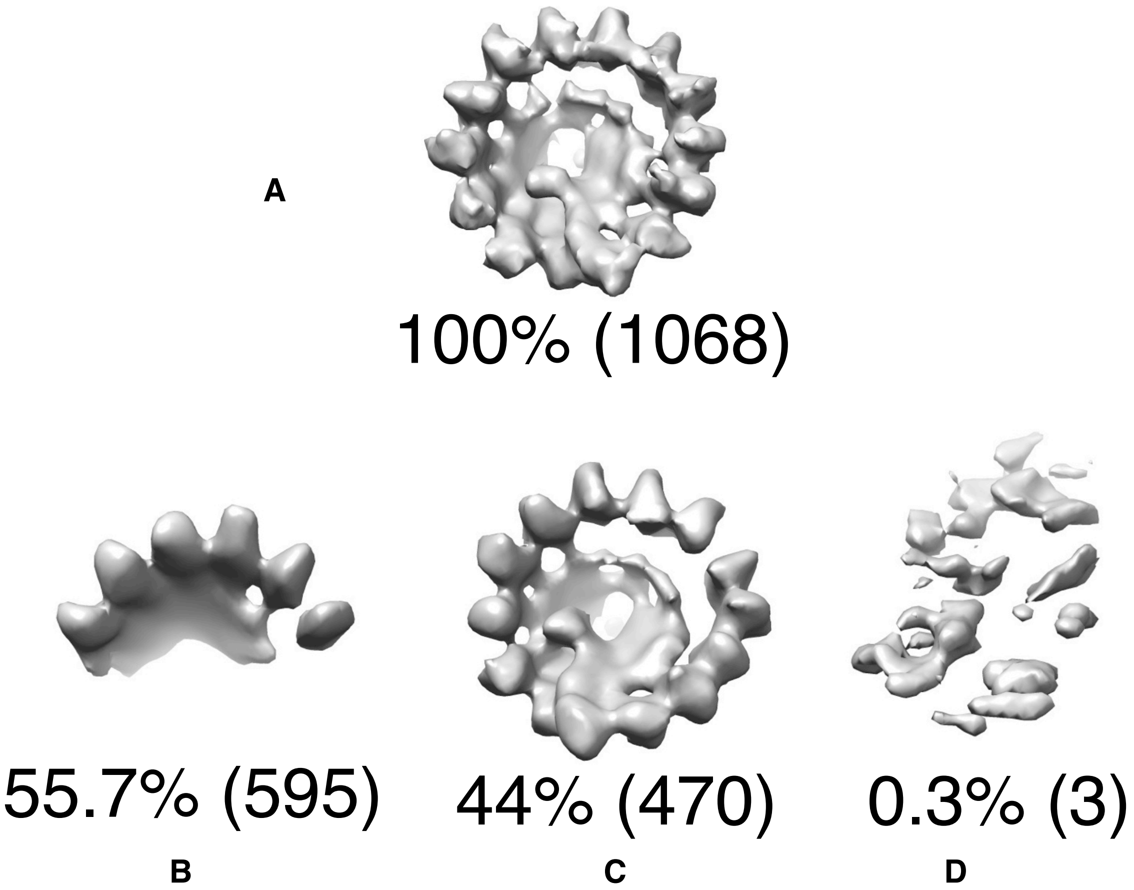

Figure 9: Initial classification of γTuRC. The average of all classes can be seen in figure (A). When divided into 3 classes, (B) has the majority of the population of particles (C) is the second largest and (D) are not a significant part of the population. In parenthesis are the number of particles in each class.

For future directions, it is necessary to overcome the orientation bias of the γTuRC in the grid in order to obtain a higher resolution structure. While this will help with the anisotropy of the structure, a big issue remains with the fact that the γTuRC is broken. To overcome this problem, bigger data sets are needed, since >50% of the particles appear broken. Another possibility is to stabilize γTuRCs with αβ-Tubulin, but this task has almost unsurmountable problems on its own.

Because of the low-resolution in the structure, it is still not possible to determine whether GCP4-6 are included in the complex. However, the extra densities that appear in the complex are constant regardless of the γTuRC prep, microscope or acquisition technique. This is a good indication that they are included; the resemblance of the γTuRC with the *S. cerevisiae* γTuRC is uncanny, and the SDS-PAGE profiles show the existence of the other GCPs in the γTuRC preps. (See Figure 10)

Section 4: Stoichiometry of *D. melanogaster* γTuRC

The stoichiometry of the *H. Sapiens* γTuRC was determined (Choi, Liu et al. 2010) using an SDS-PAGE assay. The results were based on γTuRC having one GCP5 per complex. These results can be seen in Table 2. With the advent of the structure of the *S. cerevisiae* γTuRC and the *D. melanogaster* γTuRC, it was natural to re-calculate these values based on the fact that there are 14 γ-Tubulins per γTuRC.

The assay was an SDS-PAGE stained with a fluorescent dye (Sypro-Ruby, Invitrogen) and imaged in a Typhoon scanner (GE Healthcare). The SDS-PAGE was 5 identically loaded lanes with *D. melanogaster* γTuRC pulldown with αGCP5 (Fig. 10A). The image processing was done in ImageJ (Abramoff, Magelhaes et al. 2004). The background was substracted using a rolling ball with a radius of 12. The region of interest (ROI) was selected as a rectangle that span the length of the lane. The plotted regions and picked areas can be seen in Figure 10B. The peaks were chosen based on results from Mass-Spectrometry. The resulting areas under the curve were normalized based on the molecular weight of the components. The number of subunits was determined based of 14 γ-Tubulins per γTuRC. The results can be seen in Table 2.

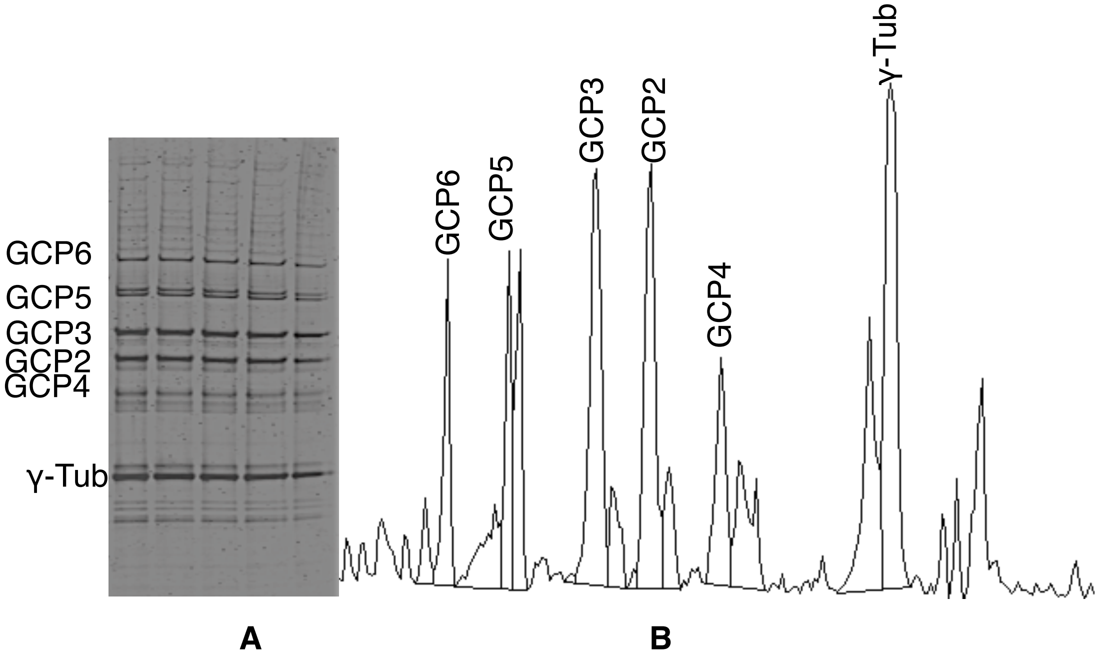

Figure 10: SDS-PAGE quantification assay of *D. melanogaster* γTuRC. (A) SDS-PAGE with background substracted. (B) Representative plot of the ROI used on the SDS-PAGE. The areas measured can be seen by lines delineating the limits.

Protein	Value±SE *H.s.*	Value±SE *D.m.*
γ-Tubulin	14.88±1.06	14.00±00
GCP4	2.59±0.40	4.04±0.5
GCP2	12.56±1.68	5.17±0.5
GCP3	12.56±1.68	5.71±0.21
GCP5	1.00±0.00	1.88±0.15
GCP6	0.56±0.02	1.4±0.07

Table 2: Stoichiometry of *H. Sapiens* and *D. melanogaster* γTuRC. *H.s.* stands for *H. Sapiens*, *D.m.* stands for *D. melanogaster* and SE stands for standard error. Values on the *H. sapiens* GCP2 and 3 are the same, because the proteins were not resolved in the SDS-PAGE.

For neither, the *D. melanogaster* and *H. sapiens* γTuRC, the addition of the GCPs is 14 (to correspond in 1:1 the amount of γ-Tubulin in the complex). However, the amounts of GCP2 and GCP3 on the *D. melanogaster* is ~10; this leaves 4 GCPs to occupy the place of either GCP2 or GCP3. This is yet another indication that GCPs indeed are located in various parts of the γTuRC .

The value of GCP5 is most likely overestimated, since the pulldown was done with αGCP5; it is empirically known that in protein complexes, the amount of the protein that is being pulldown by is greater than the rest of the complex (personal correspondence with S. Petry).

In order to improve this values, more samples should be measured to have a more statistically significant population. In addition, pulldowns using αGCP other than αGCP5 should be done to be able to measure more accurately the GCP5 value.

Section 5: Methods

Purification of γTuRC from Drosophila melanogaster embryos - using aGCP5

Buffers:

H100+IGEPAL: 50mM K-HEPES (pH 7.6), 100mM KCl, 1mM $MgCl_2$, 1mM K-EGTA (pH 7.6), 0.05% IGEPAL, 1:1000 protease inhibitor cocktail (home-made), 0.1mM GTP, 1mM DTT.

H100+IGEPAL+ATP: 50mM K-HEPES (pH 7.6), 100mM KCl, 1mM $MgCl_2$, 1mM K-EGTA (pH 7.6), 0.05% IGEPAL, 1:1000 protease inhibitor cocktail (home-made), 0.1mM GTP, 1mM DTT, 5mM ATP.

H100: 50mM K-HEPES (pH 7.6), 100mM KCl, 1mM $MgCl_2$, 1mM K-EGTA (pH 7.6), 1:1000 protease inhibitor cocktail (home-made), 0.1mM GTP, 1mM DTT.

H250: 50mM K-HEPES (pH 7.6), 250mM KCl, 1mM $MgCl_2$, 1mM K-EGTA (pH 7.6), 1:1000 protease inhibitor cocktail (home-made), 0.1mM GTP, 1mM DTT.

Beads: rProteinA Fast Flow from GEHealthcare. ProteinA FastFlow are in a 50mg/mL concentration and 400uL have 20mg capacity.

Prep - Day 1 at noon:

1) Thaw **116mL** of 1:1 fly embryo extract in a 37° water bath
2) Transfer extract to 2 Type 45 tubes on ice. Spin in a 42K rpm at 4°C for 1h and 40 min in Type45 rotor.

3) Remove lipid layer from top and transfer supernatant to 3-60mL plastic Avanti 25.5 rotor tubes, keep track of volume.

4) Add 30% PEG-8000 in H100 to clarified extract to final concentration of 2% and mix**.** Incubate on ice for 30 min.

5) Spin 20 min at 34500xg in Avanti 25.5 rotor. Discard supernatant and **resuspended pellet in 35mL** of H100+IGEPAL using a glass and teflon pestle. **Resuspended for 8 min** until pellet is completely dissolved.

6) **Transfer resuspended pellet into 2 Type 50.2 tubes on ice.** Spin for 20min at 42K rpm in ultracentrifuge.

7) Transfer clarified supernatant to 50mL conical and add 8ug of aGCP5 per mL of clarified supernatant. Tumble at 4^{o}C for 2h.

8) **Add 400uL (final)** of cleaned (in H100+IGEPAL) Protein A sepharose (GEhealthcare). Tumble at 4^{o}C for 1.5h.

9) Collect flow-through and wash 3 times: 5mL with H100+IGEPAL+5mM ATP (incubate for 15 minutes), 5mL with H100+IGEPAL+5mM ATP, 12mL with H250 and 10mL with H100.

10) Prepare 800uL of 3mg/mL Dgrip128 peptide solution (H100) for elution. After final wash, add 400uL of peptide solution and let it flow through, the add 400uL for **o/n incubation**.

<u>Prep - Day 2:</u>

11) Elute gTuRC (elution #1) and add H100 to column. Collect elution #2.

12) Take samples for SDS-PAGE and EM.

Antibody purification

Buffers:

1X PBS

1X PBS with 0.1% Triton X-100

Buffering solution: 0.15M NaCl, 0.2M Glycene-HCl pH 2.0

Storing column buffer: 1X PBS + 0.05% NaN_3

Equilibrate column and buffers at RT

Day 1:

1) Wash peptide column with 4CV

2) Thaw and dilute 1:1 rabbit serum and filter through a 0.22µm filter

3) Load column and recirculate overnight using a peristaltic pump

Day 2:

1) Wash with 5CV 1X PBS

2) Wash with 10CV 1X PBS 0.1% Triton X-100

3) Wash 5CV with 1X PBS

4) Prepare 25 - 1.5mL tubes with 50µL of 1M Tris, pH 9.5

5) Elute with 0.15M NaCl, 0.2M Glycine-HCl, pH 2.0. Collect 25mL - 1mL fractions

6) Wash with 1X PBS until pH is equilibrated, around 5CV

7) Wash column with 1X PBS + 0.05% NaN_3 and store at 4ºC

8) Check which fractions had protein by spotting 2uL of sample onto a nitrocellulose paper and stain with ponceau S stain. Pool all fractions that stained.

9) Set dialysis in 1L 1X PBS x 2 for 2h each and then 2L overnight

Day 3:

1) Concentrate pooled samples down to ~2mg/mL and dilute with glycerol by 50%. Store at -20ºC

Protein prep protocol for Drosophila γTuRC^{-mzt1} from baculovirus infected insect cells

H100+IGEPAL: 50mM K-HEPES (pH 7.6), 100mM KCl, 1mM $MgCl_2$, 1mM K-EGTA (pH 7.6), 0.05% IGEPAL, 1:1000 protease inhibitor cocktail (home-made), 0.1mM GTP, 1mM DTT.

H100+IGEPAL+ATP: 50mM K-HEPES (pH 7.6), 100mM KCl, 1mM $MgCl_2$, 1mM K-EGTA (pH 7.6), 0.05% IGEPAL, 1:1000 protease inhibitor cocktail (home-made), 0.1mM GTP, 1mM DTT, 5mM ATP.

H100: 50mM K-HEPES (pH 7.6), 100mM KCl, 1mM $MgCl_2$, 1mM K-EGTA (pH 7.6), 1:1000 protease inhibitor cocktail (home-made), 0.1mM GTP, 1mM DTT.

H250: 50mM K-HEPES (pH 7.6), 250mM KCl, 1mM $MgCl_2$, 1mM K-EGTA (pH 7.6), 1:1000 protease inhibitor cocktail (home-made), 0.1mM GTP, 1mM DTT.

Beads: anti-FLAG M2 sepharose from Sigma

1) Add 40mL of H100+IGEPAL to cells, scrape them with a spatula until thawed and put in homogenizer; pestle until no visible clumps. Save some lysate for westerns.

2) Emulsiflex it for 5 minutes or until the lysate looks clear.

3) Spin for 45 minutes at 45K rpm in Ti45 rotor at 4ºC. Wash FLAG resin.

4) Add beads and mix for 2h at 4oC

5) Wash resin with 10CV of H100+IGEPAL, 10CV of H250 and 10CV of H100. Collect washes.

6) Incubate samples with 2mg/mL 3XFLAG peptide in H100 for 30 minutes. Collect Elution #1, incubate for 10 minutes and collect Elution #2, repeat until elution #5

After this process, a second column can be added for cleaner sample. Same procedure applies to Ni-NTA beads and Strep-tactin beads.

Bibliography

Abramoff, M. D., P. J. Magelhaes and S. J. Ram (2004). "Image processing with ImageJ." Biophotonics International **11**(7): 36-42.

Chen, H., D. D. Hughes, T. A. Chan, J. W. Sedat and D. A. Agard (1996). "IVE (Image Visualization Environment): a software platform for all three-dimensional microscopy applications." J Struct Biol **116**(1): 56-60.

Choi, Y. K., P. Liu, S. K. Sze, C. Dai and R. Z. Qi (2010). "CDK5RAP2 stimulates microtubule nucleation by the gamma-tubulin ring complex." J Cell Biol **191**(6): 1089-1095.

Fernandez, J., S. Li and R. Crowther (2006). "CTF determination and correction in electron cryotomography." Ultramicroscopy **106**(7): 587-596.

Heymann, J. B. and D. M. Belnap (2007). "Bsoft: image processing and molecular modeling for electron microscopy." J Struct Biol **157**(1): 3-18.

Kollman, J. M., J. K. Polka, A. Zelter, T. N. Davis and D. A. Agard (2010). "Microtubule nucleating gamma-TuSC assembles structures with 13-fold microtubule-like symmetry." Nature **466**(7308): 879-882.

Kremer, J. R., D. N. Mastronarde and J. R. McIntosh (1996). "Computer visualization of three-dimensional image data using IMOD." J Struct Biol **116**(1): 71-76.

Li, X., P. Mooney, S. Zheng, C. R. Booth, M. B. Braunfeld, S. Gubbens, D. A. Agard and Y. Cheng (2013). "Electron counting and beam-induced motion correction enable near-atomic-resolution single-particle cryo-EM." Nat Methods **10**(6): 584-590.

Ludtke, S. J., P. R. Baldwin and W. Chiu (1999). "EMAN: semiautomated software for high-resolution single-particle reconstructions." J Struct Biol **128**(1): 82-97.

Moritz, M., M. B. Braunfeld, V. Guénebaut, J. Heuser and D. A. Agard (2000). "Structure of the gamma-tubulin ring complex: a template for microtubule nucleation." Nat Cell Biol **2**(6): 365-370.

Sorzano, C. O., R. Marabini, J. Velazquez-Muriel, J. R. Bilbao-Castro, S. H. Scheres, J. M. Carazo and A. Pascual-Montano (2004). "XMIPP: a new generation of an open-source image processing package for electron microscopy." J Struct Biol **148**(2): 194-204.

Zheng, Q. S., M. B. Braunfeld, J. W. Sedat and D. A. Agard (2004). "An improved strategy for automated electron microscopic tomography." J Struct Biol **147**(2): 91-101.

Chapter IV:

Automated Data Collection for Single-Particle Electron Microscopy Tomography with Dose Fractionation

Preface

The following chapter is work done in collaboration with Shawn Zheng. We developed an acquisition scheme to decrease tomography collection time by half (“One Sweep Acquisition”). We also included Dose Fractionation to correct for image blurring due to specimen motion during the exposure.

Shawn Zheng implemented the scheme for both the One Sweep Acquisition and the Dose fractionation, and did the initial testing with a grating replica waffle grid. I prepared, acquired and processed the Tomography on a biological sample, which was the *D. melanogaster* γ-TuRC. Shawn also quantified and modeled the specimen motion. In addition, Shawn wrote 90% of the following manuscript, including most of the figures, and I added 3 figures along with the section on the biological sample experiment and I edited the manuscript.

Abstract

Challenging structures need three-dimensional (3D) classification, yet to obtain high resolution structures, a large average of homogeneous particles are needed. Therefore, it is important to significantly expand the amount and quality of tomograms acquired. To gain efficiency, we optimize the angular range allowing a single pass data collection that starts from low end tilt (–30°) to high end (+60°). We have dubbed this acquisition scheme as “One-sweep scheme”.

Since all auxiliary operations are performed at –30° including target selection and relocation, we avoid the tracking of targets from 0° to the starting angle; this improves the robustness, and significantly speeds data collection. In order to increase the resolution of individual tomograms, critical to obtain reliable 3D classification and precise 3D alignment, we use a single electron counting direct detection camera (K2 Summit direct detection camera, Gatan, Pleasanton) for image acquisition. These direct detector cameras increase the tomogram resolution because of its superb detective quantum efficiency (> 80%). Because of the detector's ability to readout subframes during the course of exposure, and because of the recent development of precise subframe alignment, we can correct image blurring caused by the beam induced motion during exposure. The improved UCSF Tomography software package provides users not only an efficient data collection suitable for single particle electron microscopic tomography but also the ability to record and process dose fractionated tilt series. We present here, a dose fractionated tilted series collected in range of [–30°, +60°]. Despite the angular limitation, the reconstructed motion corrected volume shows improved signal to noise ratio as compared to the volume generated without the motion correction.

Introduction

Cryo electron microscopic tomography (cryo-EMT) is a well-established technology for three-dimensional (3D) analysis of biological structures of various scales in their native state. This great versatility has made cryo-EMT the method of choice in studies of a broad range of structures spanning from intact cells, and viruses to macromolecular assemblies. By contrast with single particle cryo-electron microscopy (cryo-EM) that is premised on reconstructing a 3D map from a large number of identical particles having different orientations, cryo-EMT excels in revealing structures of unique or heterogeneous samples because all the tilted information is acquired from and for each sample. However, the incomplete angular measurement intrinsic to Cryo-EMT, i.e. the so-called missing wedge, combined with the very low signal in each tilted view significantly limits attainable resolution to around 5-10nm (Grunewald, Medalia et al. 2003, Ben-Harush, Maimon et al. 2010); this represents an order of magnitude lower than the highest resolution of 3.3Å achieved by cryo-EM (Zhang, Jin et al. 2010, Li, Mooney et al. 2013). More recently, there has been great interest in those cases where the object contains distinct features or components that are heterogenous across copies. This has led to the emergence of single particle EMT (SP-EMT) as a promising tool that integrates cryo-EMT and cryo-EM in the 3D context. Tomographic volumes are first obtained by cryo-EMT and individual components or complexes are identified and subvolumes extracted. The subvolumes corresponding to randomly oriented components are then aligned in 3D and averaged. Provided that sufficient subvolumes can be obtained, this should fully correct for missing data and substantially enhance resolution. Reported resolutions from averaging 100s-1000s of copies are around 2-3nm (Liu, Bartesaghi et al. 2008, White, Bartesaghi et al. 2010, Li, Fernandez et al. 2012). One pioneering study was able to average ten thousand subvolumes, yielding a resolution of 8Å (Bartesaghi, Lecumberry et al. 2012).

To facilitate averaging, we need to significantly expand the number of tomograms obtained. Many tilt series are likely discarded during the subsequent screening and alignment process following the data collection, leaving only a fraction to be reconstructed. The generated tomograms are further screened for subvolume averaging. Therefore, successful 3D averaging is first dependent upon the acquisition of a large number of tilt series. A higher throughput data collection scheme would be highly advantageous. While increasing the number of subtomograms that can be averaged would provide a substantial improvement, resolution in SP-EMT is still quite limited by the poor signal to noise on each image. The latter is especially severe as the total allowable dose needs to be spread over the total number of tilts typically spanning ±60° in 1-2° increments. In addition, each image is contaminated by readout noise from the CCD camera. Several strategies are typically used to help counteract the low signal: rather high total doses (50-100 $e^-/Å^2$), lower magnifications to accumulate more signal in each pixel, and high values of defocus to increase contrast. The recent development of a disruptive camera technology has the potential to dramatically improve resolutions obtainable by SP-EMT. The K2 Summit (Gatan, Pleasanton) Direct Detection camera detects the incident electrons in the silicon without a scintillator, and is optimized for single electron counting. Counting has two major advantages over conventional CCD cameras and other direct detection cameras that accumulate charge throughout the exposure: electron detection increases detective quantum efficiency to > 80%, and most importantly, eliminates noise generated by the statistical deposition of charge in response to each primary electron event (Landau noise) (Li, Mooney et al. 2013). This combination results in nearly noiseless detection of electrons; this is ideally suited for tomography where the maximum allowable number of electrons that accumulate in any one pixel is low, making the resultant image utility strongly dependent on detection efficiency and camera noise.

Using the ability of direct detection cameras to readout subframes during the course of an exposure has led to the appreciation of the severity of beam-induced motion during single particle data collection (Brilot, Chen et al. 2012, Li, Mooney et al. 2013). The combination of the nearly noiseless detection of the K2 camera with a new algorithm has allowed the individual subframes to be aligned to sub-pixel accuracy, resulting in a remarkable restoration of isotropic high resolution information, and a 3.3Å reconstruction of a 700KDa protein complex (Li, Mooney et al. 2013).

Here, we show that by reducing the blurring caused by mechanical and beam-induced motions on tilted samples, dose fractionation and image alignment can also significantly aid the recording of cryoEMT data. Further, we develop an optimized automated SP-EMT data collection scheme that significantly improves throughput by building the sample map at -30° and then collecting all data in a single pass from -30° to +60°. Importantly, both these technologies are now incorporated into UCSF Tomography without compromising the existing robustness and user friendliness. As part of the entire effort, supporting procedures that automate precise stage movement and accurate setting of eucentric height have also been improved.

New collection paradigm

UCSF Tomography enables fully automated sequential acquisition of numerous data sets in a session that may span multiple days (Zheng, Matsuda et al. 2009). This was achieved by combining the multiscale grid scanning scheme implemented in Leginon, a single particle data collection software package (Potter, Chu et al. 1999, Carragher, Kisseberth et al. 2000, Suloway, Pulokas et al. 2005), with our predictive EMT data collection scheme (Zheng, Braunfeld et al. 2004). The major steps are given in Fig. 1. First, an atlas map is constructed by digitally putting together a series of images acquired from a low magnification raster scan of a region on the grid (typically 300μm x 300μm). Potential targets are identified on the map and a series of target images are then acquired at an intermediate magnification for further screening and recentering the targets prior to data collection. Data collection is divided into two loops. Each loop starts at 0° and collects only half of the tilt range but in the opposite tilting direction. When finished, the automated procedure for target re-centering is invoked to relocate the next target in the queue (Zheng, Matsuda et al. 2009). This workflow is sketched in Fig. 2A assuming a tilting range of ±60°.

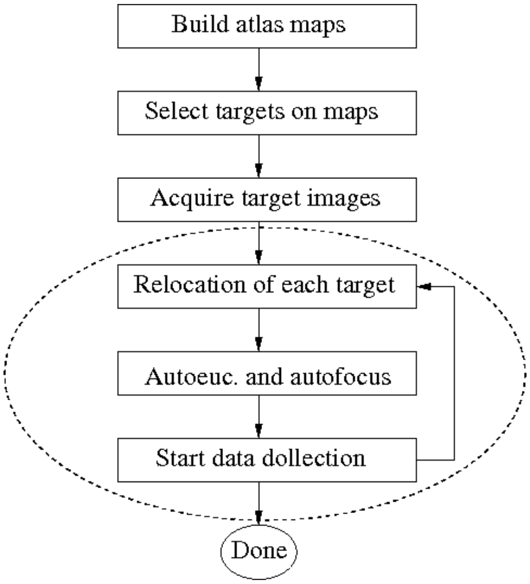

Figure 1: Major steps in automated sequential data collection. The steps within the dotted oval are the operations of sequential data collection.

The two-loop data collection was chosen because the severity of residual eucentric error is proportional to the tilt angle. Our procedure dynamically tracks sample shifts, builds a model of non-eucentricity, and predicts where the sample will be after the next tilt. However, positioning a target at the highest angle prior to data collection posed a big challenge because the shifts can be sufficient to translate the object out of the field of view. Starting at 0° provides the best tolerance for residual non-eucentricity and hence the best robustness. While the two-loop data collection has proven to be very robust, a few practical issues have been observed. First, for some data sets acquired on our FEI Polara G2 TF30 equipped with a post-column energy filter, an in-plane rotation was observed between the first 0° image and the 0° image acquired after returning from high tilt at the end of the first loop. An effective remedy was to drive the stage back to 0º in a stepwise fashion with a few seconds of relaxation at each step. While a significant improvement, this slow stepwise return slows data collection, and does not guarantee a complete elimination of the in-plane rotation; the residue still needs to be taken care in the alignment process. Second, as a consequence of dividing the data collection into two loops, the two images acquired at the beginning of each loop form a neighboring pair having a significant dose difference. In addition, diving the data can also lead to a discontinuity in the intensity distribution versus tilt angle. Although these drawbacks do not outweigh the benefits of the two-loop data collection, further suppression of their effects would be preferred.

Since SP-EMT fills the missing wedge by averaging hundreds or thousands of subvolumes, the approach is not so sensitive to the exact size of the individual missing wedge. Therefore, the tilt range of data collection could be reduced in return for speeding up the data collection as long as the resultant larger missing wedge does not pose a major challenge to the 3D classification, alignment, and averaging. Reducing the angular range also allows a higher dose to be allocated to each projection, enhancing the SNR which is important to almost every aspect of cryo-EMT and subsequent 3D averaging. Our proposed data collection scheme (Fig. 2b) aims at acquiring tilt series typically but not limited within [–30°, +60°] resulting in the same size of missing wedge as in the ±45° collection used by Bartesaghi et al., although oriented differently (Bartesaghi, Lecumberry et al. 2012). Additionally, we change the entire montage and target location to be acquired directly at the low end tilt angle and not 0°, as previously done. This completely avoids the necessity of tracking between 0° and the starting angle, improving robustness, and significantly speeding data collection. Since the autofocusing and the predicative data collection are already capable of being invoked when the stage is tilted, we will focus on changes required for constructing the tilted atlas maps, re-centering targets, and adjusting eucentric height.

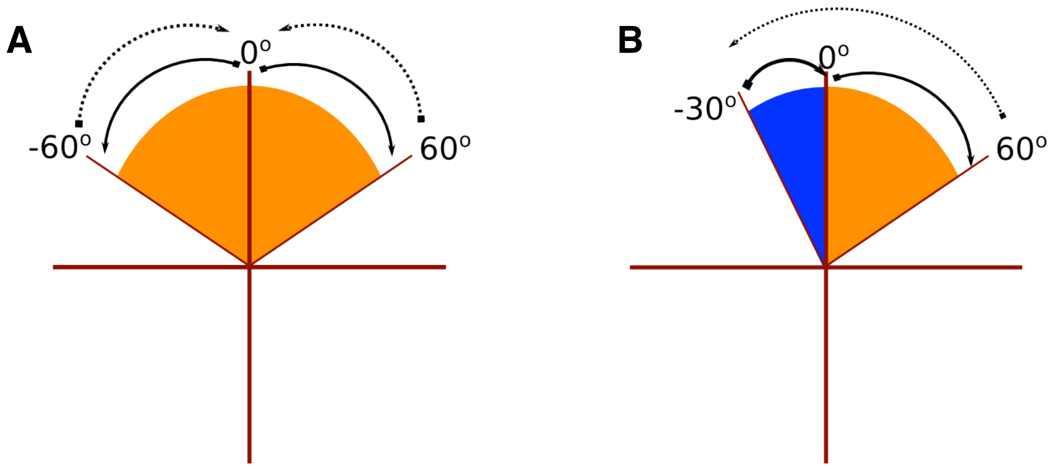

Fig. 2 Schematics of serial data collection workflow. Dotted lines represents the stage driving to the starting angle. (A) Existing data collection scheme assuming ±60° tilt range. (B) An example of the new data collection scheme in [–30°, +60°].

Stage movement along *x* and *y* axes – building a tilted atlas

Sequential data collection automatically collect numerous data sets at scattered locations on the grid that may be hundreds of microns apart, while the pixel size can be as small as a few angstroms at the magnification of data collection. Such dramatic changes in scale motivated the invention of a scheme by which a remote target is brought to the camera center in multiple steps at various magnifications (Potter, Chu et al. 1999, Carragher, Kisseberth et al. 2000, Suloway, Pulokas et al. 2005). The same strategy was adopted more recently for mapping targets before and after specimen rotation in the automated sequential acquisition of dual-axis EMT tilt series(Zheng, Matsuda et al. 2009). For sequential data collection an atlas map is first constructed by digitally stitching together a mosaic of images acquired in a raster scan of a grid region. Not only does the map present users a broad view of the grid, but it also is the first set of target coordinates that will be subsequently refined at smaller scales. In the past, atlas maps were constructed on the untilted plane because there is no stage tilting involved in the acquisition of single particle micrographs. In addition, our two-loop EMT data collection scheme always starts at 0°. Now we want to build the atlas at a non-zero end angle. Atlas maps are thus constructed on the tilted plane defined by stage *x* and *y* axes. In our past effort towards mapping the targets before and after specimen rotation for dual-axis EMT data collection, a comprehensive stage positioning procedure was developed(Zheng, Matsuda et al. 2009). A significant improvement on stage positioning accuracy was achieved by eliminating the backlash, and by adding the commonly used calibration matrix in Eq. (1) to a consistent stage movement pattern.

$$\begin{bmatrix} x_i \\ y_i \end{bmatrix} = \begin{bmatrix} \cos\theta & \sin\theta \\ -\sin\theta & \cos\theta \end{bmatrix} \begin{bmatrix} x_s \\ y_s \end{bmatrix} \quad \textbf{Eq. 1}$$

This matrix takes into account of the rotation between the stage and the image coordinates. (x_s, y_s) and (x_i, y_i) refer to the coordinates on the stage and the image planes, respectively and θ is the angle of tilt axis observed on the image plane, as is shown in Fig. 3.

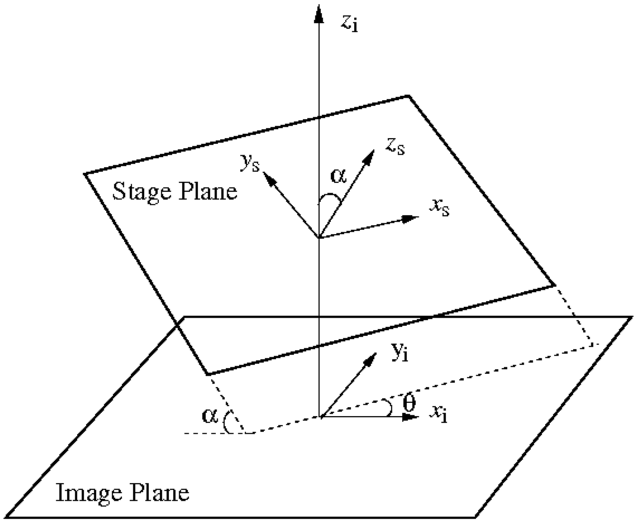

Figure 3: Tilted stage coordinate system with respect to the image plane

Since the stage is tilted, the stage plane now intersects the image plane at tilt angle α. The specimen movement along the stage *y* axis, i.e., in the direction perpendicular to the tilt axis, is a cosine projection when observed on the image plane whereas the movement along the stage *x* axis remains the same. The transformation between the stage and the image coordinates is then revised in Eq. (2):

$$\begin{bmatrix} x_i \\ y_i \end{bmatrix} = \begin{bmatrix} \cos\theta & \sin\theta\cos\alpha \\ -\sin\theta & \cos\theta\cos\alpha \end{bmatrix} \begin{bmatrix} x_s \\ y_s \end{bmatrix} \quad \textbf{Eq. 2}$$

Eq. (1) can be derived from Eq. (2) for the special case of α = 0°. Therefore, the stage tracking scheme updated with Eq. (2) is fully applicable to the untilted geometry. Three tilted atlas maps constructed at 0°, –30°, and –45°, respectively at 1700x nominal magnification on our Tecnai 20 electron microscope are shown (Fig. 4). A grating replica waffle grid (Ted Pella, USA) was used as the test specimen. Each map is 400×400 μm^2 formed by stitching 121 images of 1k×1k pixels binned 4x on hardware from the original size. As can be seen, although the higher tilt maps exhibit a little more distortions due to errors in stage positioning, their qualities are in general comparable to their 0°counterpart. Importantly, the updated scheme was found to have sufficient precision for target positioning on tilted plane at the higher magnifications where target search and relocation is performed.

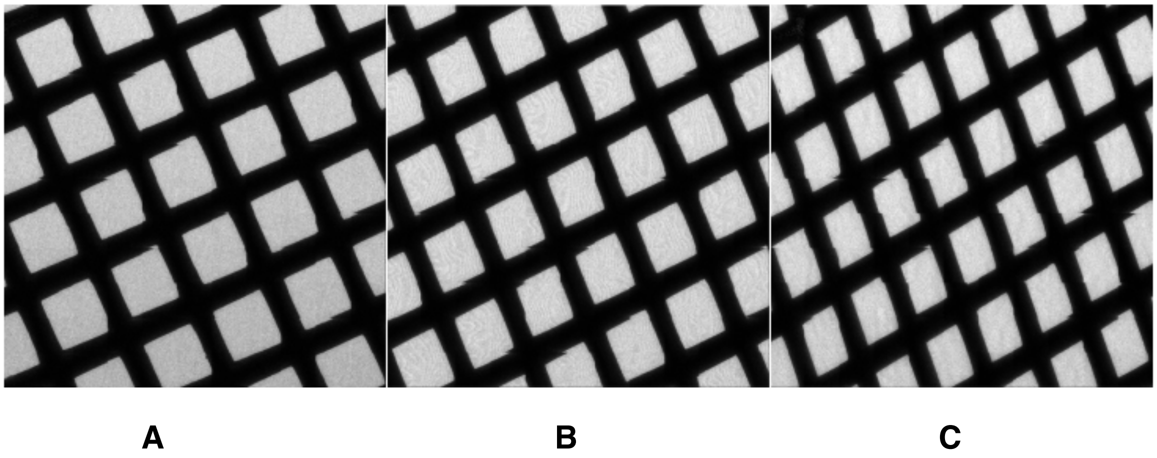

Figure 4: Atlas maps at different angles. Tilted Atlas maps of 400×400 μm^2 constructed at 1700x nominal magnification on a FEI Tecnai 20 Electron microscope equipped with a GATAN US 4000 CCD camera of 4k×4k pixels. A grating replica waffle grid was loaded with a FEI standard holder. The stage was tilted at (A) α = 0°, (B) α = –30°, and (C) α = –45° prior to the construction of each map, respectively.

Stage movement along *z* axis – eucentricity adjustment

When a specimen is tilted, the targets on one side of the tilt axis are at higher altitudes than those on the other side. The relocation of a target using XY stage movement can be described as if the target either slides downward or climbs upwards on the tilted plane to the point coincident with the camera center. This process is illustrated in Fig. 5(A). Therefore, the relocated targets are actually imaged at the same height regardless of their original original altitudes. By contrast, targets would remain at their original altitudes if they were instead relocated via image/beam shift. This scenario is sketched in Fig. 5(B). In practice, the vast majority of a specimen movement relies on the stage movement, whereas the remainder, generally due to inaccurate stage movement, is accomplished using the image/beam shift. Therefore, the targets after they are recentered in general bear different sources of eucentric error not only because of the specimen itself that may be uneven and non-uniform in thickness but, also because of their height variation as a result of inaccurate stage movements.

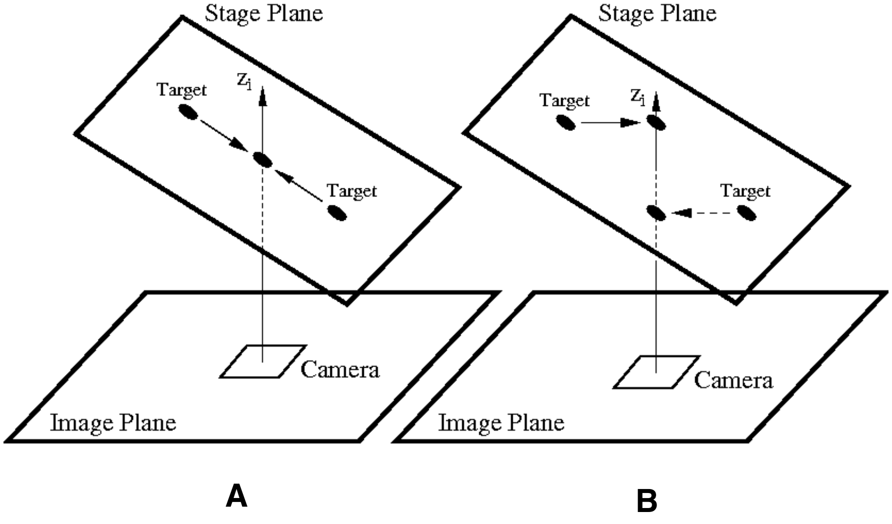

Figure 5: Altitude change: The altitude change as a result of the relocation of targets by means of (A) stage movement and (B) image beam shift.

The variation in height among relocated targets must be corrected in order to place the targets at the eucentric height and at the desired defocus settings prior to data collection. We use a variation (Zheng, Kollman et al. 2007) on the spot scan algorithm originally developed for low dose imaging of 2D crystals (Ziese, Geerts et al. 2003). This routine has now been extended to operate on any tilted plane. While the non-eucentricity (ΔZ_i) determined by means of eucentric focus measurement is in the direction of the optical axis (z_i axis), the corresponding stage z height adjustment (ΔZ_s) must factor in the projection effect of this angle and is given in Eq. (3). Additionally the change in stage z height causes an unwanted specimen shift (ΔS_i) in the image plane as given in Eq. (4). Fig. 6 presents a pair of images acquired at –30° and 14000x norminal magnification before and after –2µm of stage z height change. The image shift is about 373 pixels measured by cross correlation.

$$\Delta Z_s = \Delta Z_i / \cos\alpha \qquad \textbf{Eq. 3}$$

$$\Delta S_i = \Delta Z_s \sin\alpha \qquad \textbf{Eq. 4}$$

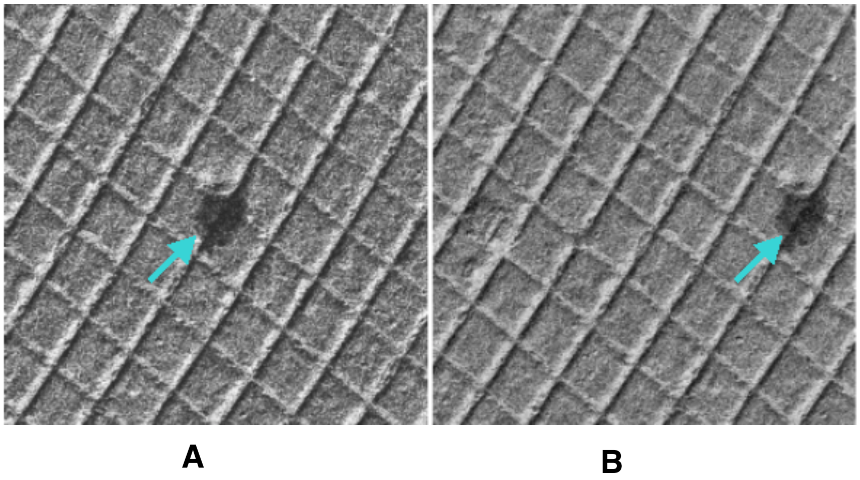

Figure 6: A pair of images acquired at –30° and 14000x nominal magnification before (A) and after (B) the stage z height was manually adjusted by –2µm. The cyan arrows show the same feature in these two images. The image shift between these two images is around 373 pixels, or 1.147µm.

By combining Eq. (3) and (4) and taking into account the projection between the stage *y* axis and the image plane, the corresponding stage *y* shift to compensate ΔS_i can be determined in Eq. (5):

$$\Delta Y_s = (\Delta Z_i / \cos\alpha)\tan\alpha \qquad \textbf{Eq. 5}$$

Our auto-eucentricity routine was updated using Eqs. (3) and (5) and tested at two different z heights distant from the eucentric point when the stage was at –30°. Two pairs of images are given in Fig. 7 showing the image shifts before and after the auto-eucentricity at 14500x norminal magnification. The eucentric error was measured around 4µm for the image pair in the top row and 10µm in the bottom row. The residual image shifts are only 34 and 128 pixels, respectively, a dramatic reduction compared to the image shift of 373 pixels stemming from only 2µm *z* height adjustment without the correction. Note that auto-eucentricity at 0° is now only a special case of this update routine since ΔZ_s is equal to ΔZ_i according to Eq. (3) and ΔZ_s is zero according to Eq. (5).

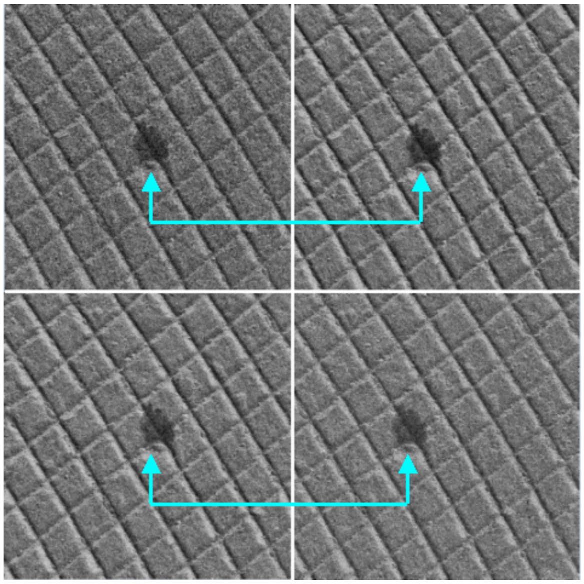

Figure 7: Two pairs of images acquired at 14500x nominal magnification at -30° stage tilt before and after the auto-eucentricity routine with the correction for the image shift being performed at around 4µm (top row) and 10µm (bottom row) away from the eucentric height. The residual image shifts are 34 pixels (top row) and 128 pixels (bottom row).

Dose fractionated tilt series

A significant concern when recording cryo tilted images is image blurring due to either mechanical stage drift or beam induced motions. For single particle studies at 0° tilt, we previously showed that the GATAN K2 Summit camera running in counting mode, combined with reading out and aligning a stack of dose fractionated subframes recorded throughout the exposure could almost completely correct mechanical and beam-induced motion (Li, Mooney et al. 2013). One limitation of electron counting is that the dose on the camera should be kept below about 8 e^-/pixel/sec to avoid scoring two electrons as a single event within the internal readout rate of 2.5 ms (400 frames/sec). Especially at lower magnifications, it can require long exposures. Given the need to fractionate the sample dose across many tilts, the exposures required to maintain this camera dose rate for tomography are typically around 2 seconds, which given the high stability of the Polara stage would not be expected to cause significant drift. By contrast, beam induced motions, especially at moderate specimen tilt, have now been found to seriously degrade image quality. Here we show that the subframes from cryo-EMT can be aligned and summed together to form an image that is nearly free of beam induced image blurring. This strategy has now been incorporated into our data collection.

As part of an ongoing project, a wild-type *Drosophila melanogaster* γ-Tubulin Ring Complex (γ-TuRC) was chosen as the test specimen. The sample was mixed with 10nm colloidal gold beads and subsequently vitrified in liquid ethane onto Rh/Cu 300 mesh Quantifoil R2/2 holey carbon films (Quantifoil, Jena, Germany) using an FEI Mark I Vitrobot. The experiment was performed on our FEI Polara G2 electron microscope using a GATAN K2 Summit direct detection camera installed before the post-column energy filter. The 3838 × 3710 pixel images were taken in counting mode at 9400x nominal magnification (4.29Å pixel size) and at an accelerating voltage of 300 kV. Each tilt series was collected in the angular range of [–30°, +60°] at every 2° with a defocus of 3.7µm and a total dose of $60e^{-}/Å^{2}$. At each angular step, the 2.5 second exposure was broken into a stack of 25 subframes, each accumulated over 0.1 second. It took about 20 min to take a dose-fractionated data set, including auxiliary operations such as target recentering, etc compared with 15 min for a regular data set without dose fractionation.

Each stack was offline-aligned based upon the algorithm developed by Li et al. (2013). The images summed from the aligned stacks were then assembled into a single MRC file according to the order of their tilt angles.

To highlight the effect of motion correction, the image in Fig. 8(A), uncorrected sum of the –30° stack extracted from a dose fractionated tilt series, is compared with the aligned sum in Fig. 8(B). As can be seen, the edge of the holey carbon film, blurry in Fig. 8(C), looks more distinct in Fig. 8(D). The Fourier transforms of these two images given in Fig. 8(E) and 8(F), respectively, also bear a significant difference. As can be seen in Fig. 8(E), a significant amount of information is lost in the region pointed by the red arrows. Since the tilt axis is 10.5° relative to the *x* axis, the information lost is mainly perpendicular to the tilt axis. In Fig. 8(F), however, the Thon ring is round and much more obvious.

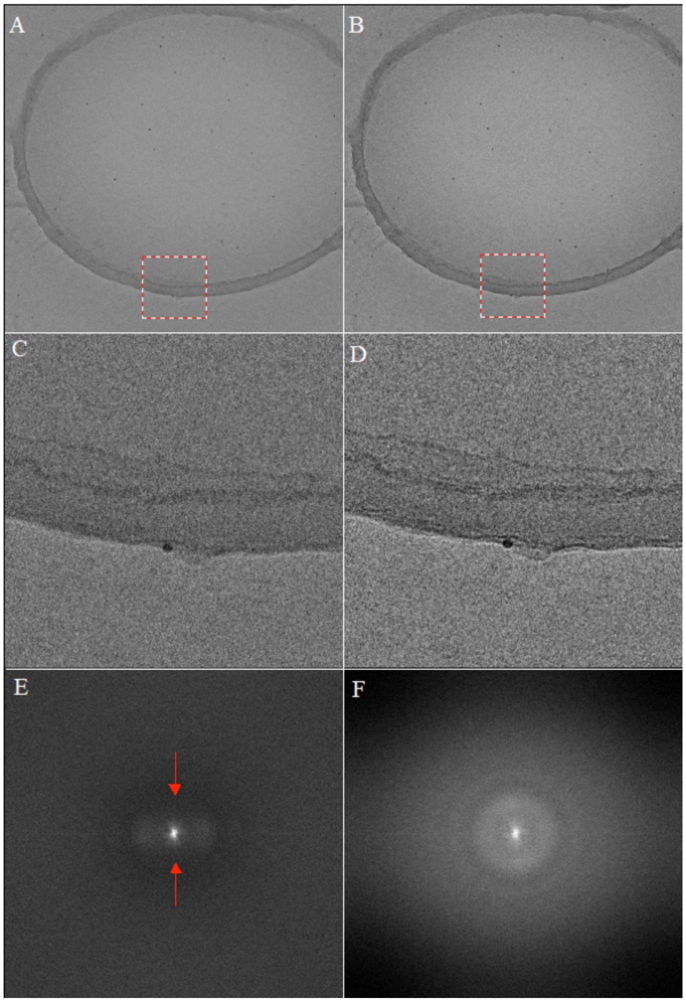

Figure 8: A pair of images summed from the same stack of subframes collected at –30° (A) before and (B) after motion correction. The boxed areas are enlarged in (C) and (D) to show the substantial improvement of the edge of the holey carbon film as a result of motion correction. (E) and (F) are used to compare the Fourier transforms of (A) and (B). The red arrows in (E) show the regions where the information are lost due to specimen motion. The full Thon rings in (F) indicate the lost information are recovered after motion correction.

In order to have a quantitative estimate of overall resolution improvement, the averaged CTFs of the entire tilt series before (Fig. 9A) and after (Fig. 9B) correction were calculated using Bsoft (Heymann and Belnap 2007). Note that prior to the CTF determination the data set was aligned using colloidal gold beads as fiducial markers in IMOD (Kremer, Mastronarde et al. 1996). The tiles of 128×128 pixels from the central stripes along the tilt axis with 50% overlap were used for the calculation. In Fig. 9(A) full Thon ring can be seen clearly at 14.0Å that is unprecedent for a single tilt series collected under cryo low dose condition (~60e$^-$/Å^2), a clear demonstration of the superb DQE as well as near noise-free electron detection provided by the K2 Summit direct detection camera. Note that the next ring at 12.7Å is partially visible mainly in the vertical direction (tilt axis). This Thon ring was fully recovered by motion correction as is shown in Fig. 9(B). Furthermore, full Thon rings can be seen clearly as far as to 11.6Å with partially visible Thon rings at higher resolution, another substantial improvement on top of the already superior resolution achieved in a single cryoEM Tomographic tilt series. There is no doubt that such a dramatic improvement of resolution in a single tilt series will have a great benefit that will propagate through entire the subsequent computations from tomographic alignment to 3D classification and 3D alignment.

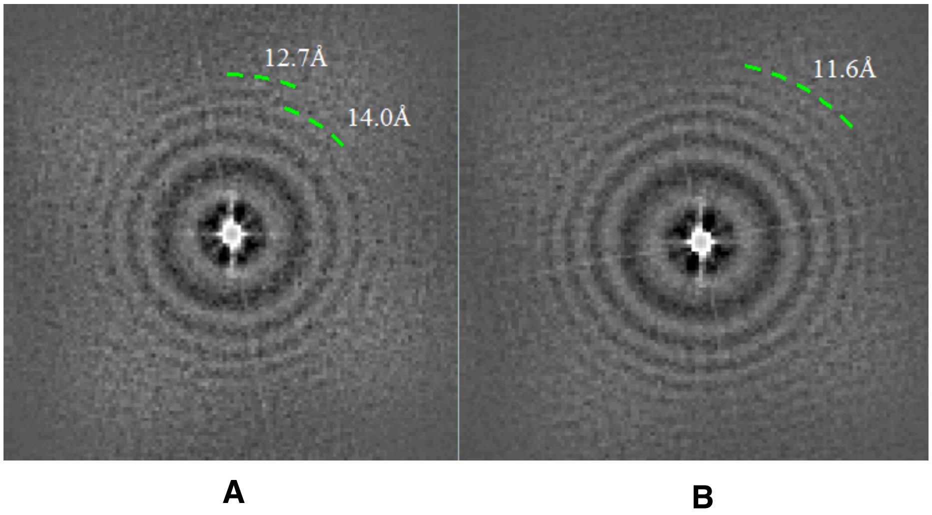

Figure 9: Averaged CTFs of a tilt series: (A) before motion correction, (B) after motion. Note that the CTFs were calculated using tiles of 128 × 128 pixels with 50% overlapping. These tiles were extracted from the central stripes along the tilt axis in each tilt image. The Thon rings are complete and distinct up to 14.0Å with an incomplete ring at 12.7Å in (A). By contrast, the Thon rings can be clearly seen as far as to 11.6Å in (B).

Traces of motion throughout the 2.5 sec exposure are shown in Fig 10(A) at three different sample tilts (-30°, 0°, 60°) with the starting points at (0, 0) labeled with a solid dot. Since the motion was found closely related to the tilt axis, the orientation of the tilt axis, 10.5° relative to the *x* axis, is also illustrated. Apparently, not only does the motion become more significant at higher tilts, but it also reverse the direction when the stage is tilted in the different side of 0°. It can be seen that the motion is found mainly perpendicular to the tilt axis and consistent with the horizontal (perpendicular to the tilt axis) blurring seen in Fig. 8(B). To verify this observation, the maximum shift vectors measured at each tilt angle are decomposed into the parallel and perpendicular components with respect to the tilt axis, see Fig. 10(B). It is found that the parallel components are no more than 2.3 pixels (9.9 Å), much smaller than the perpendicular components with the maximum magnitude of 12.9 pixel (55.3Å) observed at 60°. The variation of the perpendicular components with respect to tilt angle fit reasonably well the sine function given in Fig. 10(B). Note that the measured movement is the projection of the specimen motion that can be decomposed into three components of which one is the motion out of the tilted plane. The other two are in-plane motion along and perpendicular to the tilt axis. The in-plane motion perpendicular to the tilt axis, when measured on the image plane, is the cosine projection. The out-of-plane motion corresponds to the sine projection. This reasonable fit combined with the much smaller motion detected along the tilt axis therefore suggests that the beam induced motion is mainly the out-of-plane motion of which the maximum magnitude is approximately independent of tilt angle. It is worth noting that measurements performed on different cryo specimens using our post-GIF K2 Summit camera are similar to theses observations. Although the accumulated sample dose/tilt is very low (1.3e⁻/Å²), the magnitude of the motion at 0° is comparable to what was measured under the dose of 35e⁻/Å² by Li et al (2013, Fig. 9). A dose reduction by a factor of 27 is still unable to reduce the beam induced motion. This phenomenon is consistent with the observation of Typke et al (Typke, Gilpin et al. 2007).

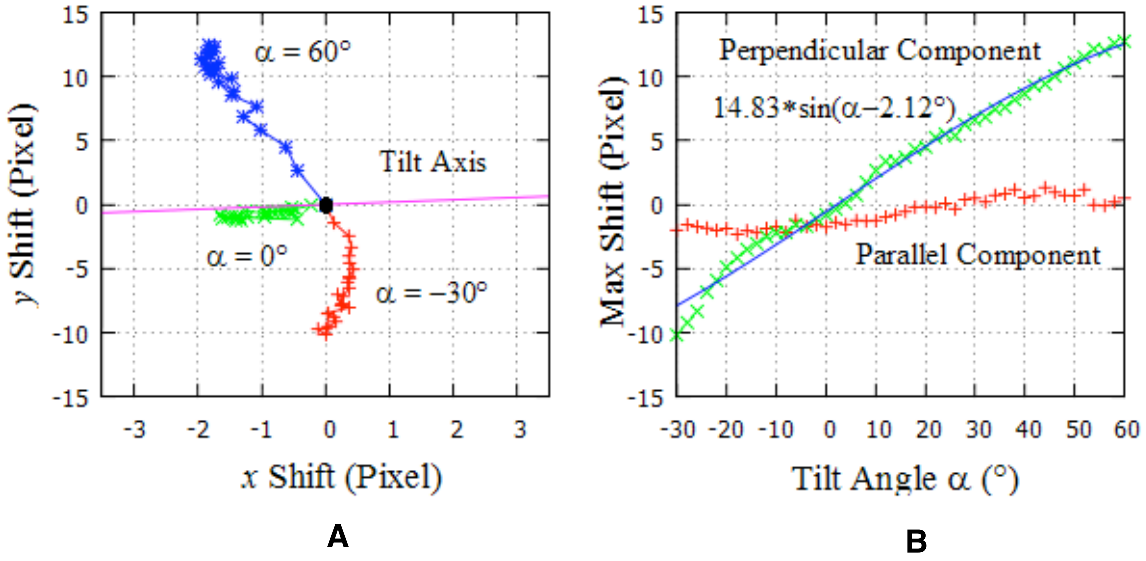

Figure 10: Motion traces (A) Traces of specimen motion measured at three tilt angles (-30°, 0°, 60°). The solid dot at (0, 0) denotes the starting point of each trace. The measured motion are found mainly perpendicular to the tilt axis. (B) The maximum motion measured at each tilt angle is decomposed into components parallel and perpendicular to tilt axis. The perpendicular components are fit to the sine function 14.83 ∗ sin(α–2.12°).

Both the motion corrected and the uncorrected tilt series were reconstructed. The corresponding *xz* slices are given in Fig. 11. Prior to reconstruction, the alignment was performed using colloidal gold beads as fiducial markers in IMOD (Kremer, Mastronarde et al. 1996). These two data sets were then CTF corrected (Fernandez, Li et al. 2006, Heymann and Belnap 2007) and reconstructed using Priism (Chen, Hughes et al. 1996). Although the γ-TuRC in different orientations are clearly seen in both Fig. 11(A) and 11(B), the structures in Fig. 11(B) are better defined with more details. For example, in Fig. 11(B) the individual γ-tubulin subunits in the complex are much more distinct, as can be seen in the γ-TuRCs with the blue and red arrows. In the case of the yellow and red arrows, one can make out the entire ring in the motion corrected data set but not quite in Fig. 11(A).

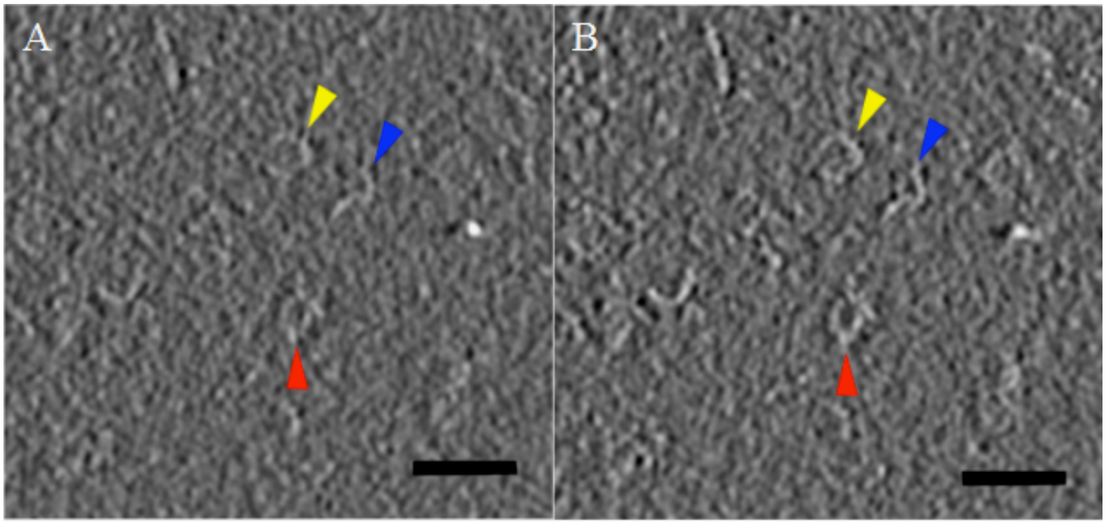

Figure 11: Sections of a reconstructed data set. (A) Non-motion corrected section (B) Motion corrected section. Image sections are binned 2x and a parzen filter with an applied cutoff of 0.25. Arrows show the ~2.2MDa γ-TuRCs in different orientations. Scale bar is 50nm.

Summary

By means of integrating 3D averaging into the context of cryo-EMT, single particle EMT has emerged as a promising, and increasingly used tool for the structural analysis of complex biological assemblies. Success of the method depends upon the accumulation of a very large number of high quality data sets in order to recover the missing data and surmount the very low signal to noise rations of each image. Two principle challenges are surmounting the very low signal to noise inherent in each image and being able to collect 100s-1000s of tomograms to allow the 3D averaging of 1000s-10000s of particles. The recent development of the GATAN K2 Summit direct detection camera, combined with the recording and accurate alignment of dose fractionated “movies” has led to breakthrough resolution enhancement for single particle cryo-EM. Here we show that this camera technology can also have a great impact on single particle EMT, especially at high tilts where motion blurring can be quite significant. The ability to record and process dose fractionated series has been integrated into UCSF Tomography software package. In an effort to improve tomogram acquisition speed without compromising robustness, we developed a new single pass data collection scheme using a limited angular range [-30°,+60°]. To optimize efficiency, all features are mapped and selected in the context of the starting tilted image. As an example and part of an ongoing project, a dose fractionated tilt series was collected within [–30°, +60°] in 2° steps for the wild-type Drosophila melanogaster γ-Tubulin Ring Complex (γ-TuRC). At each tilt, 25 subframes (3838 × 3710 pixels) are recorded at 0.1 second intrevals, and the whole set took 20 min to acquire. Motion correction substantially improved the individual images, the number of Thon rings visible and the quality of the final reconstruction. It should be emphasized that the much improved SNR on each image, propagates throughout the subsequent processing including 3D alignment, classification, and averaging.

Acknowledgements

This work was supported by funds from the Howard Hughes Medical Institute and the W.M. Keck Advanced Microscopy Laboratory at UCSF.

Bibliography

Bartesaghi, A., F. Lecumberry, G. Sapiro and S. Subramaniam (2012). "Protein secondary structure determination by constrained single-particle cryo-electron tomography." Structure **20**(12): 2003-2013.

Ben-Harush, K., T. Maimon, I. Patla, E. Villa and O. Medalia (2010). "Visualizing cellular processes at the molecular level by cryo-electron tomography." J Cell Sci **123**(Pt 1): 7-12.

Brilot, A. F., J. Z. Chen, A. Cheng, J. Pan, S. C. Harrison, C. S. Potter, B. Carragher, R. Henderson and N. Grigorieff (2012). "Beam-induced motion of vitrified specimen on holey carbon film." J Struct Biol **177**(3): 630-637.

Carragher, B., N. Kisseberth, D. Kriegman, R. A. Milligan, C. S. Potter, J. Pulokas and A. Reilein (2000). "Leginon: an automated system for acquisition of images from vitreous ice specimens." J Struct Biol **132**(1): 33-45.

Chen, H., D. D. Hughes, T. A. Chan, J. W. Sedat and D. A. Agard (1996). "IVE (Image Visualization Environment): a software platform for all three-dimensional microscopy applications." J Struct Biol **116**(1): 56-60.

Fernandez, J. J., S. Li and R. A. Crowther (2006). "CTF determination and correction in electron cryotomography." Ultramicroscopy **106**(7): 587-596.

Grunewald, K., O. Medalia, A. Gross, A. C. Steven and W. Baumeister (2003). "Prospects of electron cryotomography to visualize macromolecular complexes inside cellular compartments: implications of crowding." Biophys Chem **100**(1-3): 577-591.

Heymann, J. B. and D. M. Belnap (2007). "Bsoft: image processing and molecular modeling for electron microscopy." J Struct Biol **157**(1): 3-18.

Kremer, J. R., D. N. Mastronarde and J. R. McIntosh (1996). "Computer visualization of three-dimensional image data using IMOD." J Struct Biol **116**(1): 71-76.

Li, S., J. J. Fernandez, W. F. Marshall and D. A. Agard (2012). "Three-dimensional structure of basal body triplet revealed by electron cryo-tomography." EMBO J **31**(3): 552-562.

Li, X., P. Mooney, S. Zheng, C. R. Booth, M. B. Braunfeld, S. Gubbens, D. A. Agard and Y. Cheng (2013). "Electron counting and beam-induced motion correction enable near-atomic-resolution single-particle cryo-EM." Nat Methods **10**(6): 584-590.

Liu, J., A. Bartesaghi, M. J. Borgnia, G. Sapiro and S. Subramaniam (2008). "Molecular architecture of native HIV-1 gp120 trimers." Nature **455**(7209): 109-113.

Potter, C. S., H. Chu, B. Frey, C. Green, N. Kisseberth, T. J. Madden, K. L. Miller, K. Nahrstedt, J. Pulokas, A. Reilein, D. Tcheng, D. Weber and B. Carragher (1999). "Leginon: a system for fully automated acquisition of 1000 electron micrographs a day." Ultramicroscopy **77**(3-4): 153-161.

Suloway, C., J. Pulokas, D. Fellmann, A. Cheng, F. Guerra, J. Quispe, S. Stagg, C. S. Potter and B. Carragher (2005). "Automated molecular microscopy: the new Leginon system." J Struct Biol **151**(1): 41-60.

Typke, D., C. J. Gilpin, K. H. Downing and R. M. Glaeser (2007). "Stroboscopic image capture: reducing the dose per frame by a factor of 30 does not prevent beam-induced specimen movement in paraffin." Ultramicroscopy **107**(2-3): 106-115.

White, T. A., A. Bartesaghi, M. J. Borgnia, J. R. Meyerson, M. J. de la Cruz, J. W. Bess, R. Nandwani, J. A. Hoxie, J. D. Lifson, J. L. Milne and S. Subramaniam (2010). "Molecular architectures of trimeric SIV and HIV-1 envelope glycoproteins on intact viruses: strain-dependent variation in quaternary structure." PLoS Pathog **6**(12): e1001249.

Zhang, X., L. Jin, Q. Fang, W. H. Hui and Z. H. Zhou (2010). "3.3 A cryo-EM structure of a nonenveloped virus reveals a priming mechanism for cell entry." Cell **141**(3): 472-482.

Zheng, Q. S., M. B. Braunfeld, J. W. Sedat and D. A. Agard (2004). "An improved strategy for automated electron microscopic tomography." J Struct Biol **147**(2): 91-101.

Zheng, S., J. Kollman, M. Braunfeld, J. Sedat and D. Agard (2007). "Automated acquisition of electron microscopic random conical tilt sets." Journal of Structural Biology **157**(1): 148-155.

Zheng, S. Q., A. Matsuda, M. B. Braunfeld, J. W. Sedat and D. A. Agard (2009). "Dual-axis target mapping and automated sequential acquisition of dual-axis EM tomographic data." J Struct Biol **168**(2): 323-331.

Ziese, U., W. J. Geerts, T. P. Van Der Krift, A. J. Verkleij and A. J. Koster (2003). "Correction of autofocusing errors due to specimen tilt for automated electron tomography." J Microsc **211**(Pt 2): 179-185.

Chapter V:

Future directions

This manuscript details the work done on Microtubule nucleating complexes, both in *S. cerevisiae* and *D. melanogaster.*

The work done in *S. cerevisiae* determined the orientation of the GCP2 and GCP3 in the γTuSC, as well as showing the value of covalent tags for localization in EM. The orientation of the GCPs in the complex is thought to be conserved and it has helped the understanding of the arrangements and function of these proteins.

While big strides have been made in the structure of the *S. cerevisiae* γTuRC, with the advent of subnanometer structures, the structure of the *D. melanogaster* γTuRC remains somewhat elusive. The current structure, at a resolution of ~34Å, has 2 problems. One of the problems is the anisotropy in the structure (Chapter III, Figure 8A) which is clearly visible when compared to the *S. cerevisiae* structure. It is unclear if the problem is due to interactions with the air-water interface. It might be possible to solve the air-water interface interactions by adding a small percentage of detergent (personal communication from Kliment Verba).

The second problem is the heterogeneity in the complex caused by dissociation of the components or “breakage of the complex”. This problem can be present in the sample and it can be solved by obtaining more data, but in this case the broken complexes represent more than half the population. While it feasible, it is nevertheless a challenge. It is unclear if γTuRCs can be stabilized biochemically during the purification or by adding αβ-Tubulin, which would select those “intact” γTuRCs to grow protofilaments from. Several attemps have been made to select intact γTuRC with αβ-Tubulin and none have been fruitful.

The current *D. melanogaster* γTuRC structure, hints that GCP4-6 can be incorporated into the ring. This is clearly seen by the similarity in density with the *S. cerevisiae* γTuRC and at the appearance of extra densities where GCP2 and GCP3 are missing. In addition, the SDS-PAGE assays also hint at using GCP4-6 to take the place of either GCP2 and GCP3. One way to determine the location of GCP4-6 is to do Mass Spectrometry. An ongoing collaboration with the Chait Lab at Rockefeller entails cross linking of the γTuRC and finding neighboring peptides. While the nature of the γTuRC prep has presented with difficult challenges in terms of sample preparation, great strides have been made and early data already shows a relationship between GCP6 and GCPWD. This seems to be a feasible road to start understanding the arrangements of the *D. melanogaster* γTuRC.

Because of the challenges presented by the *D. melanogaster* γTuRC, and with the advent of the K2 Summit Direct Electron Detector a new acquisition scheme was developed. This acquisition scheme, dubbed "One-sweep" provides serial cryo-EMT collection with a time savings of ~20% from conventional cryo-EMT serial collections. In addition, dose fractionation was included in the scheme for the first time in cryo-EMT. Dose fractionation allowed to mitigate the sample movement due to interactions with the grid, making almost all datasets usable.

While this was a great stride, the same experiments should be repeated with a test sample, like GroEL so that reconstructions can be easily done and the compelling argument for using it can be made.

Publishing Agreement

It is the policy of the University to encourage the distribution of all theses, dissertations, and manuscripts. Copies of all UCSF theses, dissertations, and manuscripts will be routed to the library via the Graduate Division. The library will make all theses, dissertations, and manuscripts accessible to the public and will preserve these to the best of their abilities, in perpetuity.

Please sign the following statement:

I hereby grant permission to the Graduate Division of the University of California, San Francisco to release copies of my thesis, dissertation, or manuscript to the Campus Library to provide access and preservation, in whole or in part, in perpetuity.

Rebecca Choy
Author Signature

12/20/13
Date